arXiv:1411.7882v1 [cond-mat.stat-mech] 28 Nov 2014

Crossing the bottleneck of rain formation

M. Rohloff, T. Lapp and J. Vollmer†

Max Planck Institute for Dynamics and Self-Organization (MPI DS), 37077 Göttingen, Germany

Faculty of Physics, Georg-August Universität Göttingen, 37077 Göttingen, Germany

(Received 1 December 2014– 1:47am)

The demixing of a binary fluid mixture, under gravity, is a two stage process. Initially droplets, or in general aggregates, grow diffusively by collecting supersaturation from the bulk phase. Subsequently, when the droplets have grown to a size, where their Pèclet number is of order unity, buoyancy substantially enhances droplet growth. The dynamics approaches a finite-time singularity where the droplets are removed from the system by precipitation. The two growth regimes are separated by a bottleneck of minimal droplet growth. Here, we present a low-dimensional model addressing the time span required to cross the bottleneck, and we hence determine the time, Δt, from initial droplet growth to rainfall. Our prediction faithfully captures the dependence of Δt on the ramp rate of the droplet volume fraction, ξ, the droplet number density, the interfacial tension, the mass diffusion coefficient, the mass density contrast of the coexisting phases, and the viscosity of the bulk phase. The agreement of observations and the prediction is demonstrated for methanol/hexane and isobutoxyethanol/water mixtures where we determined Δt for a vast range of ramp rates, ξ, and temperatures. The very good quantitative agreement demonstrates that it is sufficient for binary mixtures to consider (i) droplet growth by diffusive accretion that relaxes supersaturation, and (ii) growth by collisions of sedimenting droplets. An analytical solution of the resulting model provides a quantitative description of the dependence of Δt on the ramp rate and the material constants. Extensions of the model that will admit a quantitative prediction of Δt in other settings are addressed.

Key words: Condensation/evaporation; Reacting multiphase flow; Mixing and dispersion; Low-dimensional models

1. Introduction

Precipitation emerges when aggregates, i.e. droplets, bubbles or solid particles that are immersed in a fluid, grow to a size where their motion is affected by buoyancy. At this point their motion changes from Brownian diffusion to Stokes settling, and the collision cross section increases dramatically. As a consequence aggregate growth is boosted (Houghton 1959; McGraw & Liu 2003; Grabowski & Wang 2013), collective effects emerge in their motion (Cau & Lacelle 1993; Kalwarczyk *et al.* 2008; Stevens & Feingold 2009; Woods 2010), and virtually all volume condensed on the aggregates is precipitating out of the fluid in a finite time (Cau & Lacelle 1993; Aarts *et al.* 2005; Kostinski & Shaw 2005). Precipitation is prevalent in natural processes, such as clouds (Houghton 1959; McGraw & Liu 2003; Stevens & Feingold 2009; Tokano 2011), hot- (Ingebritsen & Rojstaczer 1993; Toramaru & Maeda 2013) and cold-water (Han *et al.* 2013) geysers, as well

† Email address for correspondence: juergen.vollmer@ds.mpg.de

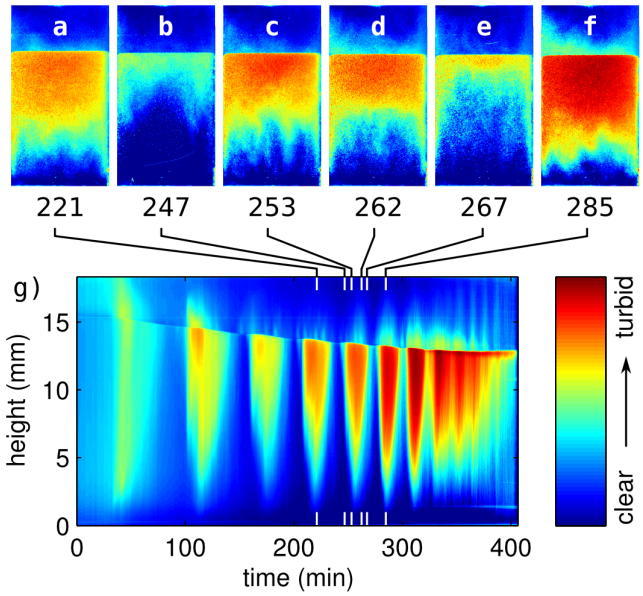

FIGURE 1. **Episodic precipitation in binary mixtures.** Panels a–f show false-colour plots of the turbidity distribution in snap shots of the phase separation of an isobutoxyethanol/water mixture subjected to a ramp rate, $\xi = 2.5 \times 10^{-5}\,\mathrm{s}^{-1}$. Averaging in horizontal direction and arranging the resulting vertical turbidity profiles next to each other produces a space-time plot of the time evolution of the turbidity, panel g. The length scale is provided on its ordinate axis, and the scales in the pictures a)–f) can be inferred by noticing that panel g shows the full height of the samples. In section 2 we provide full details on the experimental setup and method, and in Movie 1 we supply the full evolution in the false colours presented here, together with an animation illustrating the construction of the space-time plot.

as lake (Zhang 1996; Zhang & Kling 2006) and volcano (Wylie *et al.* 1999; Cashman & Sparks 2013) eruptions and the subsequent cooling of magma domes (Martin & Nokes 1988; Koyaguchi *et al.* 1990; Sparks *et al.* 1993). Moreover, it is also essential to many technical processes, like synthesis of large colloidal particles (Nozawa *et al.* 2005), steel processing (Yuan *et al.* 2004; Rimbert *et al.* 2014), and food science (Scholten *et al.* 2008; Zhang & Xu 2008).

In spite of the abundance of applications, there are many unresolved issues in the quantitative description of precipitation. For instance, a better understanding of rain formation has been identified as one of the key ingredients of improved models for climate modeling (Grabowski & Wang 2013; Blyth *et al.* 2013) and small-scale weather prediction (Stevens & Seifert 2008). Here, we present a comprehensive set of experimental data that allows us to critically survey the parameter dependence of the time scale Δt for rain formation. Data are provided for two binary fluid mixtures where demixing is driven by a continuous temperature ramp. When the ramp induces a constant generation of material, characterised by a constant value of the ramp rate, ξ, we observe repeated waves of aggregate nucleation, growth and precipitation (figure 1). We denote these waves of precipitation as *episodic precipitation*. The defining feature of episodic precipitation is an oscillatory evolution of the aggregate size distribution and of the precipitation rate in response to a slow continuous mass or heat flux into a fluid mixture. The flux leads to aggregate nucleation and growth, and episodic release of the accumulated material by precipitation events. The modulations of the precipitation rates has been observed in

laboratory experiments where phase separation in a binary fluid was monitored during pressure release (Soltzberg *et al.* 1997) or a temperature ramp (Mirzaev *et al.* 2010; Auernhammer *et al.* 2005; Lapp *et al.* 2012).

Constant driving, ξ, induces periodic waves of precipitation in both coexisting phases (figure 1). We identify the time scale Δt for rain formation as the period of the episodic response in the observed demixing. Hence, we obtain comprehensive data sets for the dependence of the time scale Δt on the viscosity, the diffusion coefficient, the mass density contrast, the number density of aggregates and the driving. The latter all vary over several orders of magnitude in our experiments (cf. appendix A).

The data on Δt is compared to a low-dimensional model that accounts for diffusive growth of small aggregates, and a crossover to collection-dominated growth for large aggregates. The model differs from classical models of rain formation by modeling the diffusive growth according to state-of-the-art models for nanoparticle synthesis (Sugimoto 1992; Tokuyama & Enomoto 1993; Leubner 2000; Clark *et al.* 2011), rather than adapting classical Ostwald ripening (Houghton 1959; Wilkinson 2014). We will show that these assumptions are sufficient to quantitatively predict the values of Δt for the demixing of binary fluid mixtures, and to faithfully capture the dependence of the period on their material constants, the number density of droplets and the ramp rate.

For the demixing of binary fluid mixtures the time scale, Δt, is selected by a bottleneck arising at the crossover from the diffusive growth of small aggregates to growth dominated by collection of other aggregates. The crossover emerges once the motion of the largest aggregates is affected by buoyancy. All applications mentioned above share conditions where the overall droplet volume is growing in time. Under these conditions the diffusive growth is typically dramatically faster than for classical Ostwald ripening, i.e. in circumstances where the overall droplet volume is preserved and the droplet number decays like one over time. Indeed, for all experimentally accessible ramp rates, $\xi > 0$, droplet growth progresses at a constant aggregate number density (Sugimoto 1992; Leubner 2000; Tokuyama & Enomoto 1993; Clark *et al.* 2011; Vollmer *et al.* 2014). The focus of the present paper will therefore be the characterisation and modeling of aggregate growth and precipitation in settings with a sustained constant growth speed ξ of the overall aggregate volume fraction, and the analysis of the dependence of Δt on ξ, the aggregate concentration n, and appropriate material constants.

The paper is organised as follows: In section 2 we provide details on the considered mixtures, and the experimental procedure to determine Δt. It culminates in the presentation of a large data set that clearly establishes a strong dependence of Δt on the ramp rate ξ. The robust features of episodic precipitation call for a universal description of the oscillation period. Such a theory is established in section 3. The resulting prediction is in very good quantitative agreement with the experimental data. (All material constants needed for the quantitative comparison are provided in appendix A.) The model allows us to revisit problems encountered in quantitative descriptions of warm terrestrial rain (section 4): diffusive droplet growth in a classical Ostwald-like scenario is too slow to account for the observed time scale, Δt. In contrast, our new model provides estimates for clouds that are too fast. We attribute this to simplifications of the droplet collision kernel that are well-justified for binary mixtures with relatively small settling rates, but that substantially overestimate the growth rate in systems, like terrestrial rain, with large density contrast of the coexisting phases. We conclude in section 5 with a summary of our main results, and a discussion of extensions of the model that will allow us to address precipitation arising in other settings.

2. Experiment

We will discuss the parameter dependence of Δt for repeated waves of precipitation in two well-controlled laboratory experiments: mixtures of isobutoxyethanol/water and of methanol/hexane that are subjected to a range of different temperature ramps. The system is contained in a light scattering cuvette and its temperature is controlled by immersion in a water bath so that we have full control over external perturbations. In our experiment, figure 1, two partially miscible liquids form two layers with a phase which is richer in the less dense fluid floating over a layer of the high-density phase. The temperature of the mixture is varied smoothly away from the phase coalescence point, T_c, and the time-dependence of the temperature is engineered so that the ramp rate, ξ, of the droplet volume fraction remains constant in each run of the experiment. A movie illustrating the corresponding temperature evolution together with a video of the sample is provided in movie 2. In response to the ramp both layers show an alternating variation in turbidity, figure 1.a)–f) and figure 2.c). Representing this evolution in a space-time plot, figure 1.g), illustrates a variation of turbidity with a period Δt_i between the i^{th} and $(i+1)^{\text{st}}$ precipitation event. The accompanying periodic alternation in the turbidity and the particle size distribution are characteristics of episodic precipitation. The effect is robust. Episodic response has been observed in the particle size distribution (Lapp *et al.* 2012) and in calorimetric data (Vollmer *et al.* 1997; Vollmer & Vollmer 1999; Auernhammer *et al.* 2005; Mirzaev *et al.* 2010) in a vast range of binary mixtures (Vollmer *et al.* 1997; Auernhammer *et al.* 2005; Mirzaev *et al.* 2010; Lapp *et al.* 2012), including olive oil and methylated spirit (Vollmer *et al.* 2007). It arises in the upper as well as in the lower layer of the mixtures.

2.1. *Experimental Setup*

Figure 2.a) shows the experimental setup. The sample cell (1), a 3 mL fluorescence cell 117.100F-QS made by Hellma GmbH, is illuminated by a KL 2500 LCD Schott cold light source (2) such that dark-field images can be taken with a BM-500CL monochrome progressive scan CCD camera (3). The camera takes 772×1420 pixel images of the sample cell with a frame rate between 0.1 and 3 Hz depending on the ramp rate ξ.

The sample temperature is controlled by immersion into a water bath that follows a temperature protocol imposed by a computer-controlled thermostat (4): an immersion cooler Haake EK20 is cooling with constant power, and a Huber CC-E immersion thermostat is heating the water bath to the preset temperature. Additionally, the temperature of the water near the sample is measured with a PT100 temperature sensor. The temperature is controlled with an accuracy of 15 mK. Homogenisation for repeated runs is provided by a magnetic stirring unit (5).

The inset (1a) in figure 2.a) shows a magnification of the sample cell. The camera captures the turbidity of the full cell, providing 8 bit turbidity data as shown in figure 2.c). Averaging this data in horizontal direction and plotting the resulting scans of the turbidity height profiles, provides the space-time plot figure 2.b). For visual inspection the contrast in these pictures is conveniently enhanced by a representation in false colours, figure 1. As supplementary online material we provide movies showing the black-and-white turbidity data taken by the camera together with a plot of the time evolution of the temperature, Movie 2, and an animation, Movie 1, illustrating the construction of the space-time plot of the turbidity shown in figure 1.g).

The space-time plots, figures 1.g) and 2.c), clearly visualise the period Δt between subsequent waves of precipitation. Episodic precipitation goes along with marked oscillatory changes in the droplet size distribution (Lapp *et al.* 2012), and in the turbidity of

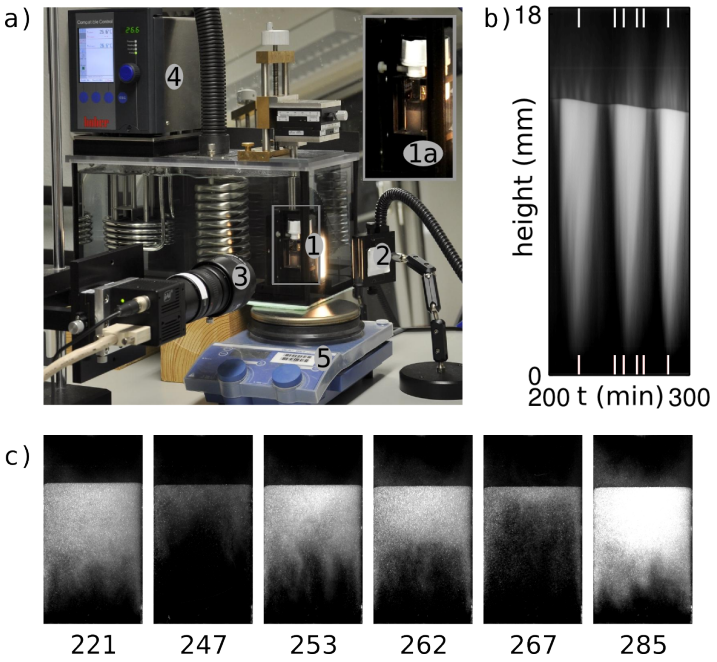

FIGURE 2. **Setup and raw data obtained from the CCD camera.** a) Photo of the experimental setup. Its components, (1)–(5) are described in the main text. b) Space-time plot based on the turbidity data provided by the camera. The sample contains a mass fraction of 0.2751 isobutoxyethanol in water, and was subjected to a ramp rate $\xi = 2.5 \times 10^{-5}\,\mathrm{s}^{-1}$. c) Representative snap shots of the times where the snap shots were taken are indicated below the respective photos, and by white bars in panel b). In Movie 2 we provide the full time evolution as captured by our camera.

the samples (Auernhammer *et al.* 2005). The main panels of figure 3 show representative traces of the turbidity of the samples when heated with different, constant ξ. The data for Δt are extracted from these traces as the distance between subsequent maxima of the turbidity.

In addition to capturing the turbidity we succeeded to follow the time evolution of the droplet size distribution of IBE droplets in water via an appropriately enhanced illumination and imaging (Lapp *et al.* 2012). Wherever available an analysis of the temporal evolution of the droplet size distributions along the same line as the one for the space-time plots of the turbidity, provides identical values for Δt_i with a higher experimental accuracy. Further details on the experimental setup are provided in Lapp *et al.* (2012), and the data analysis used to extract the oscillation period from the space-time plots has been described in Auernhammer *et al.* (2005).

2.2. *Investigated Mixtures*

Two types of mixtures are considered:

Methanol/hexane (M+H) These mixtures are one of the classical model systems of binary phase separation (Huang *et al.* 1974; Beysens *et al.* 1988; Abbas *et al.* 1997; Iwanowski *et al.* 2006; Sam *et al.* 2011). The two liquids are fully miscible above the critical temperature $T_c = 34.45°\mathrm{C}$. The concentrations of the coexisting phases that are

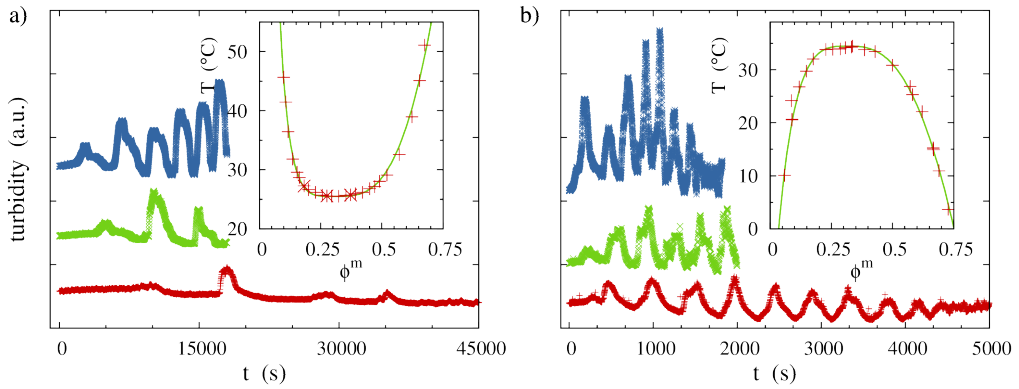

FIGURE 3. **Phase diagrams and time traces of the turbidity.** The insets show the phase diagrams of a) IBE+W, and b) M+H, and the respective main panels show oscillations of the turbidity in the lower layer for different ramp rates ξ: from top to bottom a) $2.5 \times 10^{-5}\mathrm{s}^{-1}$, $1.25\times10^{-5}\mathrm{s}^{-1}$, $5\times10^{-6}\mathrm{s}^{-1}$ for IBE+W, and b) $4\times10^{-4}\mathrm{s}^{-1}$, $2\times10^{-4}\mathrm{s}^{-1}$, $1\times10^{-4}\mathrm{s}^{-1}$ for M+H. The data points of the turbidity correspond to the average turbidity of a region of 140 μm height and the full sample width, that is located 650 μm below the meniscus. The different signals are shifted vertically for better visibility.

formed for lower temperatures are shown in the phase diagram in figure 3.b). See Abbas *et al.* (1997) for a detailed description.

Isobutoxyethanol/water (IBE+W) Mixtures of water and butoxyethanol have become popular as an experimentally-friendly system that phase separates upon heating (see e.g. Emmanuel & Berkowitz 2006). For our present purposes IBE and water, figure 3.a), is even preferential since the critical point of the mixtures, $T_c = 25.61°\mathrm{C}$, lies more than 10°C below the one of the butoxyethanol mixture. This further enhances the range of experimentally accessible temperatures (that must always lie well below the boiling point of water). See Nakata *et al.* (1982) and Lapp *et al.* (2012) for more detailed descriptions.

For the fit of the coexistence curve we follow the procedure of Aizpiri *et al.* (1990). To first order they approximate the left and right branch of the coexistence curve by

$$\Phi_{r/l} = \Phi_c \pm B\,\theta^{\beta} + D\,\theta^{2\beta} \tag{2.1}$$

with the reduced temperature $\theta = |1 - T/T_c|$, the critical point being at temperature T_c with composition Φ_c, and the universal scaling exponent $\beta = 0.325$. For the M+H mixture this provides a good fit, the solid green line, shown in the inset of figure 3.b), with fit parameters listed in Table 1. On the other hand for IBE+W the exponent $\beta = 0.325$ only applies for $\theta < 10^{-3}$ (Nakata *et al.* 1982), which is too small for our purposes. Even correction terms based on the Wegner expansion do not help (Nakata *et al.* 1982). To have a simple set of parameters we therefore choose $\beta = 0.25$, which admits a faithful description based on three free non trivial parameters (see figure 3.a) and Table 1).

The temperature ramps in our experiments amount to increasing temperature for IBE+W, and decreasing temperature for M+H. For simplicity we denote this as heating, and understand that the temperature ramp rate is negative for the latter mixture. On the other hand, the ramp rate of the droplet volume fraction, ξ, is positive in either case, as elaborated in section 2.3.

The evolution can most conveniently be described by focusing on a region in one of the macroscopic phases. Its average concentration changes due to sedimentation of large droplets. However, immediately after a precipitation event, the bulk and the remaining

	IBE + W	M + H
β	0.25	0.325
T_c [K]	298.76 ± 0.12	307.88 ± 0.15
Φ_c	0.3093 ± 0.0032	0.3143 ± 0.0008
B	0.547 ± 0.002	0.726 ± 0.002
D	0.26 ± 0.015	0.323 ± 0.005

TABLE 1. Fit parameters of the coexistence curve for IBE+W and M+H.

small droplets are very close to an equilibrium composition at points on the coexistence curve with composition Φ_b for the bulk phase, and Φ_d for the remaining droplets in the fluid. The phases occupy the volumes V_b and V_d, respectively.

As the mixture is further heated, the equilibrium concentrations of the coexisting phases change in response to the broadening of the miscibility gap, i.e. the region bounded by the coexistence curve. A temperature difference δT causes a change in the equilibrium composition by $\delta\Phi_b < 0$ and $\delta\Phi_d > 0$. It gives rise to a concentration current across the interface of the droplets, which in turn leads to a growth of the droplets. In the following subsection we review how the temperature protocol of the experiments was chosen in order to fix the ramp rate, ξ, of the droplet volume fraction.

2.3. *Calculating the ramp rate ξ*

The derivation of the ramp rate, ξ, starts from the the average composition

$$\phi = v_d \Phi_d + (1 - v_d)\, \Phi_b \tag{2.2}$$

of a small volume of a mixture, where droplets of composition Φ_d occupy a volume fraction v_d in a background phase of composition Φ_b. By definition, the average composition, ϕ, is preserved when the droplets start growing in response to a change of temperature. On the other hand droplet growth is accompanied by a change of the composition of the phases,

$$0 = \dot{\phi} = v_d\, \dot{\Phi}_d + \Phi_d\, \dot{v}_d + (1 - v_d)\, \dot{\Phi}_b - \Phi_b\, \dot{v}_d\,. \tag{2.3}$$

We introduce the notations

$$\zeta = \Phi_0^{-1}\, \frac{\mathrm{d}\bar{\Phi}}{\mathrm{d}t} \tag{2.4a}$$

$$\xi = \Phi_0^{-1}\, \frac{\mathrm{d}\Phi_0}{\mathrm{d}t} \tag{2.4b}$$

$$\varphi = \frac{\phi - \bar{\Phi}}{\Phi_0} \tag{2.4c}$$

$$\text{where} \qquad \bar{\Phi} = \frac{1}{2}\, (\Phi_b + \Phi_d)\,, \tag{2.4d}$$

$$\Phi_0 = \frac{1}{2}\, (\Phi_b - \Phi_d)\,, \tag{2.4e}$$

and substitute the resulting expressions for $\dot{\Phi}_d$ and $\dot{\Phi}_b$ into (2.3). Solving for $\dot{v}_d$ one obtains then after some straightforward algebra

$$\dot{v}_d = \frac{1}{2}\, (\zeta + \xi\varphi)\,. \tag{2.5}$$

Here, φ is the reduced average concentration defined in (2.4c). It takes the value $\varphi = 1$ when $\phi = \Phi_b$, and smaller values for compositions inside the miscibility gap.

Assuming local equilibrium one can characterise the local bulk concentration by the space dependent field $\varphi(x,t)$. Its time evolution obeys a diffusion equation with a source strength of $2\,\dot{v}_d$ (Cates *et al.* 2003). According to the above consideration this source term gives rise to a corresponding growth of the equilibrium droplet volume fraction. From the point of view of the transport equations, the magnitude of the source strength $\dot{v}_d$ appears therefore as the relevant parameter characterising how strongly the mixture is driven away from equilibrium. With this motivation we consider here temperature protocols that correspond to fixed values of $\dot{v}_d$.

In (2.4) it is understood that Φ_0 and $\bar{\Phi}$ are functions of $T(t)$ due to their dependence of Φ_d and Φ_b, i.e. on the borders of the two-phase region of the phase diagram. In general these functions have a different temperature dependence. Hence, it is not clear a priory that $\dot{v}_d$ can be fixed to a constant value by choosing an appropriate form of the temperature ramp $T(t)$. Indeed, we choose different temperature protocols for the two phases—i.e. for the M+H (and IBE+W) mixtures we adopt different temperature ramps for methanol (IBE) droplets in hexane (water) than for hexane (water) droplets in methanol (IBE). The optimal protocol is found by rearranging (2.5) to take the form

$$\dot{v}_d = \frac{1}{2\Phi_0(T)}\frac{\mathrm{d}\Phi_b}{\mathrm{d}t} - \frac{v_d}{\Phi_0}\,\frac{\mathrm{d}\Phi_0}{\mathrm{d}t} \approx \frac{1}{2\Phi_0(T)}\frac{\mathrm{d}\Phi_b}{\mathrm{d}T}\frac{\mathrm{d}T}{\mathrm{d}t}\,, \tag{2.6}$$

where the approximation in the final step is based on the fact that the volume fraction of droplets v_d is always small in our experiments. According to (2.6) the ramp rate $\dot{v}_d$ for droplets in the upper and lower layer of our samples is found by appropriately assigning the indices b and d to the respective branches of the phase diagram. Subsequently, the temperature protocol of the ramp is obtained by integrating

$$\frac{\mathrm{d}T}{\mathrm{d}t} = 2\,\dot{v}_d\;\Phi_0(T)\;\left(\frac{\mathrm{d}\Phi_d}{\mathrm{d}T}\right)^{-1}. \tag{2.7}$$

In practice there is only a small difference between $\dot{v}_d$ and ξ since $\zeta \ll \xi$ for the phase diagrams under consideration, and since φ is always very close to one. Hence, on the one hand, we distinguish between $\dot{v}_d$ and ξ for the sake of calculating the temperature protocol. This avoids systematic errors in the numerical integration of (2.7). On the other hand, for the further presentation of the data, we specify the ramp rate in terms of ξ. This allows us to use terminology that is consistent with the pertinent literature (Cates *et al.* 2003; Vollmer & Vollmer 1999; Auernhammer *et al.* 2005; Vollmer *et al.* 2007; Lapp *et al.* 2012).

2.4. *Experimental results for* Δt

Figure 4 compiles data of Δt for a vast range of heating rates ξ, and four different scenarios of phase separation in a binary mixture: a) the emergence and sedimentation of water-rich droplets in an isobutoxyethanol-rich phase; b) the emergence and rising of isobutoxyethanol-rich droplets in a water-rich phase; c) the emergence and sedimentation of methanol-rich droplets in a hexane-rich phase; and d) the emergence and rising of hexane-rich droplets in a methanol-rich phase.

Different data points for a given ramp rate are due to the drift of Δt when pertinent material constants change upon moving further away from the critical point. In appendix A we provide the temperature dependence of the material constants, which in turn translates to a time dependence when inverting the protocol $T(t)$ of the temperature ramp. For all data the height of the layer was $h \approx 1\,\mathrm{cm}$. Measurements for samples

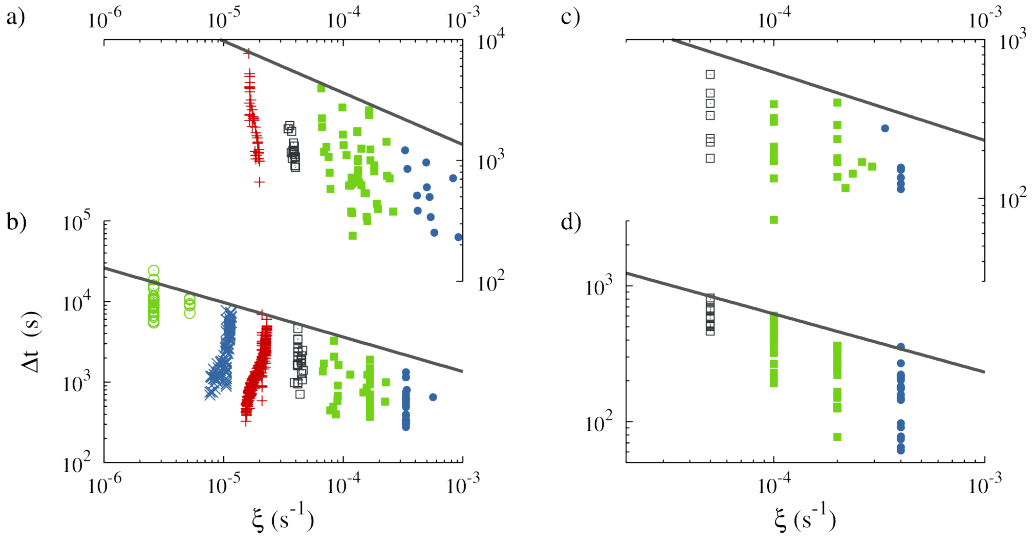

FIGURE 4. **The oscillation period, Δt, plotted vs. the ramp rate ξ.** The four panels show Δt for a) water-rich droplets in an IBE-rich continuous phase, b) IBE-rich droplets in a water-rich continuous phase, c) methanol-rich droplets in a hexane-rich continuous phase, and d) hexane-rich droplets in a methanol-rich continuous phase, respectively. The different symbols denote measurements for different ranges of ramp rates, ξ. The colours and symbols encode different heating rates ξ: open green circle, $\xi < 6\times10^{-6}\,\mathrm{s}^{-1}$; blue cross, $10^{-6}\,\mathrm{s}^{-1} < \xi < 1.3\times10^{-5}\,\mathrm{s}^{-1}$; red plus, $1.3\times10^{-5}\,\mathrm{s}^{-1} < \xi < 3\times10^{-5}\,\mathrm{s}^{-1}$; open black square, $3\times10^{-5}\,\mathrm{s}^{-1} < \xi < 6\times10^{-5}\,\mathrm{s}^{-1}$; green square, $6\times10^{-5}\,\mathrm{s}^{-1} < \xi < 3\times10^{-4}\,\mathrm{s}^{-1}$; and blue circle, $3\times10^{-4}\,\mathrm{s}^{-1} < \xi$. The grey lines are guides to the eye that indicate the slope of a power law, $\Delta t \sim \xi^{-3/7}$.

with varying heights between $h = 0.25\,\mathrm{cm}$ and $5.5\,\mathrm{cm}$ for the lower layer showed that Δt is hardly affected by h. The data points for the IBE+W mixture (left) are obtained by particle tracking (cf. Lapp *et al.* 2012 for experimental details), and those for M+H (right) refer to subsequent minima of turbidity measurements as shown in figure 3. We verified that both methods provide the same results. However, the data obtained from droplet tracking tend to be more accurate.

In the following section we establish a model for the droplet growth and sedimentation that provides a quantitative description of Δt for all data presented in figure 4.

3. Theory

As a first step to model Δt we consider the reasons why the turbidity — and hence the precipitation rate — in our experiment is not steady: the turbidity of a transparent fluid mixture increases when a considerable number of droplets have grown to a size comparable to (and eventually larger than) the wavelength of light. This manifests as a change of colour in the lower part of the cell when the system progresses from the snapshots shown in figure 1.b)–c). Conversely, the fluid becomes clearer again when vast amounts of small droplets are collected during the sedimentation of the largest droplets (transition from figure 1.d)–e)). Repetition of the cycle of nucleation, growth of droplets, and resetting the system by sedimentation gives rise to episodic precipitation, as shown in the space-time plot, figure 1.g). In the following the salient features of this dynamics are modelled.

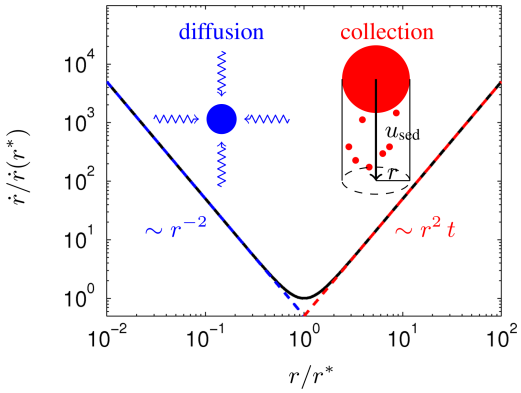

FIGURE 5. **Bottleneck in droplet growth.** As a function of droplet size r the growth speed $\dot{r}$ of droplets shows a sharp minimum at a size r^*. Smaller droplets grow by diffusion — the growth of larger droplets is speeded up by sedimentation, that promotes the collection of small droplets (see insets).

3.1. *Evolution of the radius of the largest droplets*

We start with general considerations motivating the setup of the model.

1. Spatial degrees of freedom need not be considered to describe the evolution of the largest droplets. For the nonlinear reactions terms characterising phase separation the convective mixing efficiently eliminates spatial inhomogeneities of the droplet size distribution (Benczik & Vollmer 2010, 2012). Indeed, based on visual inspection of the accompanying movies, we estimate the mixing time scale to be of the order of seconds. It is about three orders of magnitude smaller than the period Δt.

2. It is sufficient to consider the characteristic size of the largest droplets rather than the full droplet size distribution. For diffusively growing droplets the size distribution is sharply bounded towards large droplets. Consequently, the largest droplets in the system have a well-defined size and there are only few of these droplets (Slezov 2009; Clark *et al.* 2011; Vollmer *et al.* 2014). When buoyancy starts to effect their motion these large droplets collect smaller droplets, grow rapidly, and eventually clear the system from droplets by precipitation (Kostinski & Shaw 2005).

3. While many different processes contribute to the droplet growth, it suffices to consider only droplet growth by diffusive accretion that relaxes supersaturation, and the collection of small droplets by sedimenting large ones in order to achieve a quantitative description of Δt. The processes are illustrated in figure 5, and we will now discuss them in turn.

3.1.1. *Growth by diffusive accretion that relaxes supersaturation*

The dynamics of large droplets crossing the meniscus (Aarts *et al.* 2005) and droplet nucleation (Binder & Stauffer 1976; Farjoun & Neu 2011) provide microscopic droplets in the fluid. Subsequently, the supersaturation in the bulk relaxes by diffusion of the minority component onto the droplets. The diffusive accretion of material on the droplets relaxes supersaturation and induces droplet growth.

In the experiments the temperature ramp is adjusted in such a way that the volume fraction of droplets grows linearly in time with a speed ξ. For these growth conditions it was demonstrated in Sugimoto (1992); Tokuyama & Enomoto (1993); Clark *et al.* (2011); Vollmer *et al.* (2014) that the number density of droplets is preserved. Droplets

of a characteristic radius r and number density n occupy a volume fraction $n\,4\pi r^3/3$. When the droplet volume fraction increases with speed ξ and the number density n is conserved, diffusive growth provides a temporal change of the droplet radius

$$\frac{\mathrm{d}}{\mathrm{d}t}\frac{4\pi\, n\, r^3}{3} = \xi \quad \Rightarrow \quad \dot{r} = \frac{\xi}{4\pi n}\,\frac{1}{r^2}\,. \tag{3.1}$$

Alternatively, this growth law can be obtained as large k approximation of the diffusive growth law (Clark *et al.* 2011; Vollmer *et al.* 2014)

$$\dot{a} = \frac{\sigma D}{a^2}\left(k\,\frac{a}{\langle a\rangle} - 1\right), \quad k = 1 + \frac{\xi}{4\pi\sigma D n} \tag{3.2}$$

describing the growth of a droplet of radius a in an assembly of droplets with distribution $P(a)$ and mean droplet radius $\langle a\rangle = \int \mathrm{d}a\, a\, P(a)$. In (3.2) D is the diffusion coefficient for accretion of material on the droplets, and

$$\sigma = \frac{2\gamma V_m^2 C_\infty}{RT} \tag{3.3}$$

is the Kelvin length (Lifshitz & Pitaevskii 1981; Bray 1994), that depends on the interfacial tension γ, the molar volume V_m, and the equilibrium composition of the droplet phase C_∞ in units of mol/m^3. (Specific values of the material constants are provided in appendix A.) It was shown in Vollmer *et al.* (2014) that k takes values of the order to 10^6 under the conditions considered here, and that $a \simeq \langle a\rangle$ in the late stages of competitive droplet growth at large k. Hence, (3.2) reduces to (3.1).

3.1.2. *Growth by collection of smaller droplets*

When the droplets become sufficiently large, they drift under the influence of buoyancy forces. According to Stokes' formula the velocity of a slowly settling droplet is (Taylor & Acrivos 1964; Guyon *et al.* 2001)

$$u = \kappa r^2 \qquad \text{with} \quad \kappa = \frac{2}{9}\,\frac{g\,\Delta\rho}{\mu_b}\,\frac{\mu_d + \mu_b}{\mu_d + \frac{2}{3}\mu_b}\,, \tag{3.4}$$

where g is the gravitational acceleration, $\Delta\rho$ the density contrast, μ_b is the dynamic viscosity of the bulk phase, and μ_d is the viscosity of the material in the droplets. When the Stokes velocity of the the largest droplets in the system becomes noticeable they collect smaller droplets in their path. Hence, the volume of a large droplet grows like $4\pi r^2\,\dot{r} = \varepsilon\pi r^2 u\xi t$, where ε is the collection efficiency for large droplets coalescing with smaller ones, and ξt is the volume fraction of the smaller droplets. (Observe that r refers to the radius of the largest droplets in the system—a minute minority of droplets that accounts for only a small part of the droplet volume fraction.) Accordingly, we find the collisional growth rate

$$\dot{r} = \frac{\varepsilon\kappa\xi t}{4} r^2\,. \tag{3.5}$$

3.1.3. *The bottleneck of droplet growth*

The diffusive growth mechanism, (3.1), works very well for small droplets due to the factor r^{-2}, and it becomes less and less efficient when r grows. In contrast, growth by collecting small droplets, (3.5), does not contribute to the growth as long as all droplets are small, while it leads to runaway growth of the large droplets when their motion is affected by buoyancy. Hence, we assert that the sum of the diffusive growth, (3.1), and

the contribution accounting for the collection of smaller droplets, (3.5),

$$\dot{r} = \frac{\xi}{4\pi n}\frac{1}{r^2} + \frac{\varepsilon\kappa\xi t}{4}r^2\,, \tag{3.6}$$

faithfully describes the growth of the largest droplets in the system. The growth law, (3.6), shows a bottleneck of growth at the bottleneck radius, r^*, where the droplet growth speed, $\dot{r}$, takes its smallest value, $\dot{r}(r^*, t^*) = (2/3)\,(r^*)^{-2}$ (see figure 5),

$$r^* = r(t^*) \simeq (\pi n \varepsilon\kappa\, t^*)^{-1/4}\,. \tag{3.7a}$$

The bottleneck is approached at the time t^* required for droplets to grow from zero radius to the radius r^*. Integrating (3.1) from $r = 0$ to $r = r^*$ yields $4\pi n {r^*}^3/3 = \xi t^*$. Together with (3.7$a$) this equation provides the following expressions for the bottleneck time t^* and the bottleneck radius r^*,

$$t^* = \left(\frac{2^8\,\pi}{3^4}\,\frac{n}{\varepsilon^3\kappa^3\xi^4}\right)^{1/7}, \qquad r^* = \left(\frac{3}{4\pi^2}\frac{\xi}{\varepsilon\kappa n^2}\right)^{1/7}. \tag{3.7b}$$

Henceforth, we measure time in units of t^*, droplet radii in units of r^*, and, for conciseness of the notation, we denote the resulting dimensionless units still as (r, t). In terms of these dimensionless variables (3.6) takes the form

$$\dot{r} = \frac{1}{3\,r^2} + \frac{t\,r^2}{3}\,, \tag{3.8}$$

such that the growth velocity $\dot{r}(r, t)$ takes its minimum at $(r, t) = (1, 1)$.

3.2. *Calculating the period* Δt

As long as buoyancy does not yet affect the motion of the largest droplets in the system, the droplets grow diffusively by collecting supersaturation. In leading order for small droplets one can then neglect the growth contribution $tr^2/3$ in (3.8). For an initial droplet size $r(t = 0) = 0$ this entails

$$\dot{r} \simeq \frac{1}{3\,r^2} \quad \Rightarrow \quad r_S(t) \simeq t^{1/3}\,, \tag{3.9a}$$

where the index S in $r_S(t)$ stresses that the approximation applies as long as droplets are small, $r_S \lesssim 1$. As shown by the dotted line in figure 6.a) this approximation provides a good estimate for values $t < 1/2$.

Similarly, for large droplets the contribution $(3r)^{-2}$ to the growth is sub-dominant in (3.8) such that in leading order

$$\dot{r} \simeq \frac{r^2\,t}{3} \quad \Rightarrow \quad r_L(t) \simeq \frac{6}{\Delta t^2 - t^2}\,. \tag{3.9b}$$

Here, the index L in $r_L(t)$ indicates that this solution applies when the droplets are large, $r_L \gtrsim 1$. The growth law, (3.9b), features a finite-time singularity when t approaches Δt. At the latest at this late time, the large droplets will rapidly fall out of the measurement window, such that the system is reset to its initial state $r \simeq 0$. On the one hand, the dash-dotted line in figure 6.a) shows that (3.9b) provides a very good description of the numerical data for $t \gtrsim t^\star$ for the choice $\Delta t = 2.44$. On the other hand, the expression (3.9b) can not be matched continuously to (3.9a) because for $\Delta t = 2.44$ the latter expression produces smaller values for $r(t)$ for all t. Rather, a continuous and differentiable

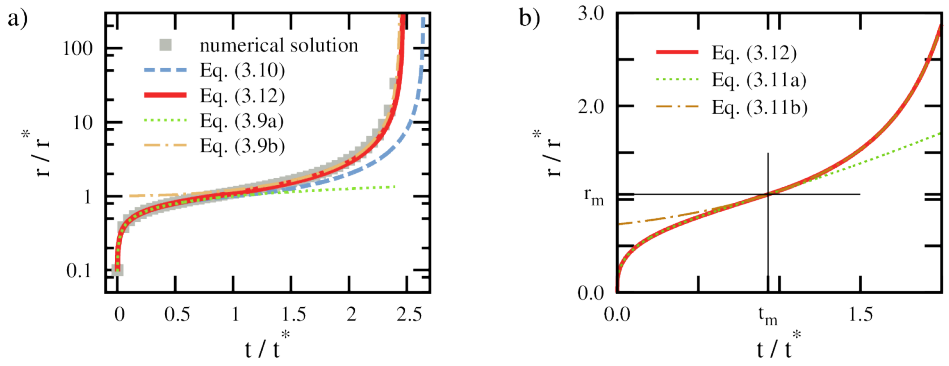

FIGURE 6. **Finite-time divergence of droplet growth.** a) Comparison of the numerical solution of (3.8) (grey squares) to the analytical approximations, (3.10) (dashed blue line) and (3.12) (solid red line), respectively. The green dotted line shows the leading order approximation for small droplets, (3.9*a*), and the brown dash-dotted lines the description of the divergence of the size of large droplets, (3.9*b*), evaluated for $\Delta t = 2.44$. The analytical description of the droplet growth, (solid red line), is also shown in panel b) which shows how (3.12) is obtained by matching the expressions (3.11*a*) and (3.11*b*) for small and large droplets, respectively.

interpolation from (3.9*a*) to (3.9*b*) requires to choose

$$r(t) \simeq \begin{cases} t^{1/3} & \text{for} \quad t \leqslant 1\,, \\ 6\,(7-t^2)^{-1} & \text{for} \quad t \geqslant 1\,. \end{cases} \tag{3.10}$$

The resulting first order estimate for $r(t)$ is shown by the dashed blue line in figure 6.a). It diverges at $\Delta t = \sqrt{7} \simeq 2.646$, thus overestimating the time Δt required to reach the finite-time singularity observed in the numerical data by about 8%.

A more accurate description of the numerical solution of (3.8) is obtained by taking into account the leading order corrections of (3.9*a*) and (3.9*b*). A refined estimate for the droplet growth is obtained by using $r_S(t)$ to approximate the sub-leading contribution to the growth of r^3 by $tr^4 \simeq t^{7/3}$. The resulting solution of (3.8) becomes

$$\frac{\mathrm{d}}{\mathrm{d}t} r^3 \simeq 1 + t^{7/3} \quad \Rightarrow \quad r_s(t) \simeq \left(t + \frac{3}{10}\, t^{10/3} \right)^{1/3} . \tag{3.11a}$$

This expression provides an excellent fit to the numerical data for $t \lesssim t^\star$, as shown by the the dotted green line in of figure 6.b).

For the large droplets a more accurate prediction is obtained by using $r_L(t)$ to approximate the $(3r)^{-2}$ term in (3.8),

$$-\frac{\mathrm{d}}{\mathrm{d}t} r^{-1} = \frac{t}{3} + \frac{1}{3}\, r^{-4} \simeq \frac{t}{3} + \frac{1}{3} \left(\frac{\Delta t^2 - t^2}{6} \right)^4$$

$$\Rightarrow\ r_l(t, \Delta t) \simeq \left[\frac{\Delta t^2 - t^2}{6} + \frac{(\Delta t - t)^5}{3 \cdot 6^4} \left(\frac{t^4}{9} + \frac{5\, t^3\, \Delta t}{9} + \frac{23\, t^2\, \Delta t^2}{21} + \frac{65\, t\, \Delta t^3}{63} + \frac{128\, \Delta t^4}{315} \right) \right]^{-1} . \tag{3.11b}$$

When evaluated at $\Delta t = 2.467$ the expressions (3.11*a*) and (3.11*b*) match continuously

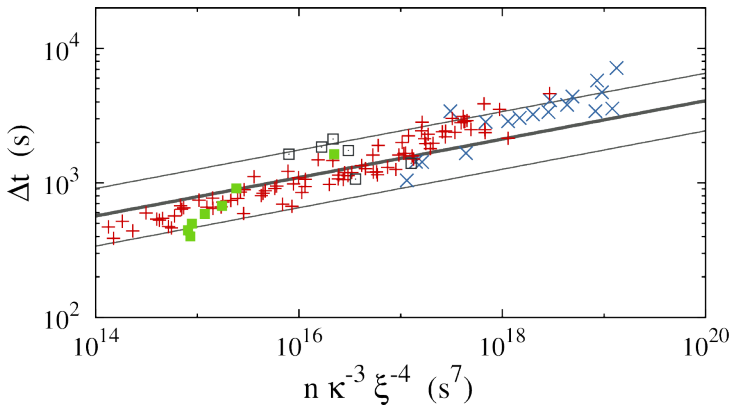

FIGURE 7. **Dependence of Δt on n, κ, and ξ.** The period of episodic precipitation in IBE+W mixtures of various compositions collapse on a curve when plotting Δt as a function of $n\kappa^{-3}\xi^{-4}$. Here, the respective heating rates in units of s^{-1} are specified in the caption of figure 4 and the measurement of the number densities, n, have been reported in Lapp *et al.* (2012). When collecting the numerical prefactors and accounting for the temperature dependence of κ, the collection efficiency, ε, remains as the only free parameter of the prediction (3.13). Varying ε induces a vertical displacement of the line. Here, ε was set to the value $\varepsilon = 0.3$ for the thick solid line. The thinner lines above and below correspond to the choices $\varepsilon = 0.1$ and $\varepsilon = 1$, respectively.

and differentiable at the point $(t_m, r_m) = (0.9304, 1.0526)$, [figure 6.b)]

$$r(t) \simeq \begin{cases} r_s(t) & \text{for} \quad t \leqslant t_m = 0.9304\,, \\ r_l(t, \Delta t = 2.4667) & \text{for} \quad t \geqslant t_m = 0.9304\,. \end{cases} \tag{3.12}$$

The thick solid red lines in both panels of figure 6 show the expression (3.12) over the full t-range. It provides an excellent description of the numerical solution of (3.8) that is shown by grey squares. In particular, the position of the predicted finite-time singularity, $\Delta t = 2.467$, is only off by one percent from the numerically obtained value, $\Delta t = 2.44$.

In conclusion, the parameter dependence of the time scale, Δt, for the growth from vanishingly small to very large droplets is provided by the time, t^*, required to grow to the bottleneck size, r^*. Based on (3.7b) and the fit of Δt in (3.9b) to match the asymptotics of the numerical data shown in figure 6, we find

$$\Delta t \simeq 2.44\, t^* \simeq 3.39 \left(\frac{n}{\varepsilon^3 \kappa^3 \xi^4}\right)^{1/7} . \tag{3.13}$$

A first hint that this prediction might be faithful is obtained by observing that the parts of a period where we observe high and low turbidity in figure 3 are of comparable extent. This is consistent with the theoretical prediction that the singularity arises at $\Delta t = 2.44\, t^*$. A more thorough test is presented in figure 7 where we plot Δt as function of $n\kappa^{-3}\xi^{-4}$. The plot is based on data of Lapp *et al.* (2012) where the time evolution of the droplet density was followed by particle tracking such that both, Δt and n, are known from the experiment. The data determining the temperature dependence of κ is provided in appendix A. Hence, the collection efficiency, ε, remains as the only free parameter of the prediction, (3.13). It induces a vertical displacement of the prediction on the logarithmic scale in figure 7. The theoretical curves displayed in figure 7 show the prediction (3.13) for the constant values, $\varepsilon = 0.1$, 0.3, and 1, respectively. These

values correspond to the middle and the respective most extreme values observed for other systems (Beard & Ochs 1993), where the collection efficiency ε was reported to take values in the range $0.1 \leqslant \varepsilon \leqslant 1$. All data points lie in the narrow band around the prediction, well within the uncertainty of ε. There only is a slight systematic mismatch of the slope. We attribute this trend to a weak temperature dependence of ε. The mismatch arises from a correlation of the temperature dependence of κ and α, and the corresponding dependence of ε.

3.3. *Accounting for different droplet densities*

Typically the droplet density, n, is not easily accessible. It is therefore desirable to provide an estimate for n in order to arrive at a widely applicable theory for the period, Δt. In the context of our experiments this can be achieved by observing that the expression k, defined in (3.2), is preserved during the periods of diffusive droplet growth (Klein & Moisar 1963; Sugimoto 1992; Clark *et al.* 2011), and that $k \gg 1$ for the present experiments (Vollmer *et al.* 2014). Hence, the number density n is proportional to $\xi/(\sigma D)$. Combining this proportionality with (3.13) we obtain

$$\Delta t = \alpha \left(D\sigma\kappa^3\right)^{-1/7} \xi^{-3/7} \,. \tag{3.14}$$

The factor α comprises numerical prefactors and the dependence of Δt on quantities that are not accessible in many circumstances: the collection efficiency, ε, and the parameter k characterising the diffusive growth. The coefficients D, σ and κ in (3.14) are functions of material constants. They show a strong temperature dependence that arises from the vanishing of the interfacial tension and the mass density contrast at the critical temperature, T_c, of the phase transition. This, in turn, entails the vanishing of σ and κ which are proportional to the interfacial tension and the mass density contrast, respectively (cf. appendix A). Hence, (3.14) suggests that $\Delta t\, \xi^{3/7}$ should be a function of the reduced temperature $\theta = |T - T_c|/T_c$. This proposition is corroborated in figure 8. It shows a remarkable data collapse for all data compiled in figure 4 when plotting $\Delta t\, \xi^{3/7}$ as function of θ. Moreover, the resulting temperature dependence is faithfully described by the master curves, (3.14). The dimensionless prefactor α is the only free parameter in this description. This parameter takes values very close to unity that only depend on the selected mixture: $\alpha = 0.71$ for IBE+W (left panels of figure 8), and $\alpha = 0.9$ for M+H (right panels of figure 8).

4. Discussion

In the present section we interpret the modeling of the data for the binary mixtures with particular emphasis on the quality of the data collapses shown in figures 7 and 8. What are the underlying assumptions? What would one expect for other systems?

4.1. *Values of α for binary mixtures*

The solid lines in figure 8 faithfully provide the θ dependence of Δt even though (3.14) only accounts for the temperature dependence of the material constants, and disregards the temperature dependence of ε and k, that should be present according to our discussion of figure 7 in section 3.2. Consequently, the dimensionless prefactor α is the only free parameter in (3.14). Comparing (3.13), (3.2) and (3.14) one finds,

$$\alpha \simeq 2.44 \left(\frac{2^6}{3^4}\right)^{1/7} (k-1)^{-1/7}\, \varepsilon^{-3/7} \,, \tag{4.1}$$

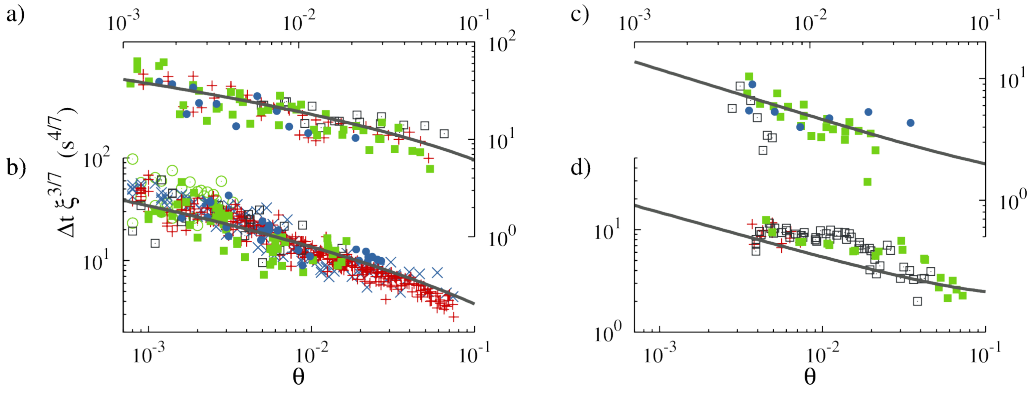

FIGURE 8. **Temperature dependence of $\Delta t\,\xi^{3/7}$ for IBE+W and M+H mixtures.** Data points are shown for the upper (top) and the lower layer (bottom) of mixtures of IBE+W (left) and M+H (right), respectively. We use the same symbols and colours as in figure 4, and show the theoretical prediction, (3.14), by solid lines. The same value of α is found for the upper and the lower layer of the mixtures, $\alpha = 0.71$ for IBE+W (left), and $\alpha = 0.9$ for M+H (right).

where 2.44 is the ratio of Δt and the bottleneck time scale t^* found by the fit of (3.9b) in figure 6. Typical values of ε are $0.1 \lesssim \varepsilon \lesssim 1$ (Beard & Ochs 1993), and for the IBE+W system Vollmer *et al.* (2014) reported $10^5 \lesssim k \lesssim 10^7$. For $k = 1.7 \times 10^5$ and $\varepsilon = 0.3$ one indeed finds the value $\alpha = 0.71$ adopted in figure 8. There is only a weak variability of α in spite of the substantial range of values taken by ε and k: the $(1/7)^{\text{th}}$ and $(3/7)^{\text{th}}$ power in (4.1) strongly suppress these dependences.

4.2. *Temperature dependence of* Δt

In contrast to a suggestion in the literature (Wilkinson 2014) we are reluctant to attribute the θ dependence of $\Delta t\,\xi^{3/7}$ to the critical scaling of the material constants entering (3.14), i.e. the dependence on D, $\sigma = 2\gamma V_m^2 C_\infty/(RT)$ and $\kappa = 2g\,\Delta\rho/(9\mu)$. The reason is fourfold:

(i) the values of θ in our experiments clearly lie outside the critical range. This is documented in the appendix A where we report a much more involved θ dependence of the material constants than the power-law singularities describing the scaling for small reduced temperatures θ;

(ii) in addition to D, σ and κ also the collection efficiency ε shows a noticeable temperature dependence, as observed in figure 7;

(iii) the parameter k entering the definition, (4.1), of α has a noticeable temperature dependence (Vollmer *et al.* 2014);

(iv) for the mixtures under consideration the dependence of ε and k cancels partially. Consequently, the close correspondence of the θ dependence of the prediction (3.14), and the one obtained by considering α to be a constant and D, σ and κ to vary according to the power laws valid very close to critical point might very well be a coincidence. A proper discussion of the temperature dependence of Δt should first address the intriguing observation that k takes surprisingly large values in the present experiments, and that the observed values vary so little that their dependence need not be considered to obtain a good estimate of the oscillation period, figure 8.

4.3. *Bottleneck radius*

Figure 9 shows the time evolution of the distribution of the droplet volume fraction $v(r,t)$ of droplets of radius r. Panel a) provides an overview in terms of a radius vs. time plot

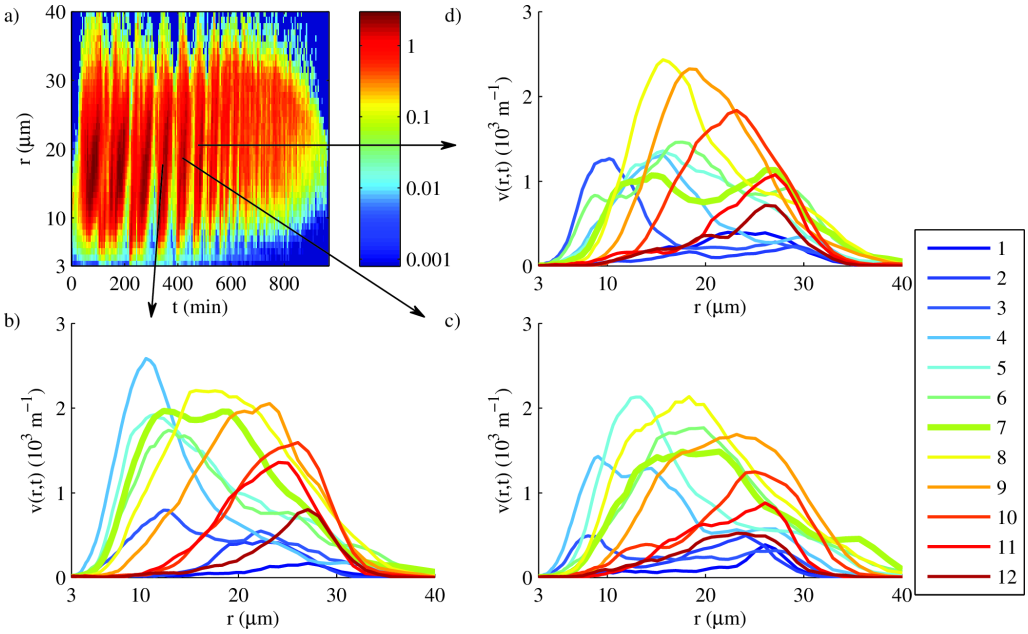

FIGURE 9. **Evolution of the droplet size distribution** for the lower layer of the IBE+W mixture subjected to a ramp rate of $\xi = 1.05 \times 10^5 \mathrm{s}^{-1}$. a) A radius-time plot of the distribution of the droplet volume fraction $v(r,t)$ clearly captures the oscillations in time. b–d) explicitly provide the radial distribution of the volume fraction for the fourth, fifth and sixth oscillation. To suppress fluctuations the distributions are determined as temporal averages over one of twelve time intervals of equal length in each oscillations. Within each period the distributions at different times are labelled by a colour coding ranging from blue to red, as specified in the legend. The thicker green lines, number 7, correspond to the time where the bottleneck is crossed.

where $v(r,t)$ is indicated by false colour. Each of the panels b)–d) shows twelve curves that describe the evolution of the distribution during one oscillation. In the beginning of each period there is a pronounced peak for small radii (blue lines). The maximum of the distribution shifts to larger radii as the distribution evolves, it develops a shoulder (curve 3–5), becomes bimodal (thick green curve 7), and then the number of large droplets rapidly decays (curves 8–12). We attribute the decay to precipitation. The arising of the shoulder reflects the broadening of the distributions when the largest droplets have crossed the bottleneck (Beard & Ochs 1993; Kostinski & Shaw 2005). From this perspective the minimum arising in the bimodal droplet spectra should amount to the bottleneck radius, r^*. For the data of measurements in the lower layer of IBE+W, that are shown in figure 9, the bottleneck radius is thus found to lie in the range $r^* \simeq 15 \ldots 20\,\mu$m [cf. the thick green curves, number 7, in figure 9.b)–d)]. This experimental observation matches exactly the radius calculated based on (3.7*b*). Indeed, for the data shown in figure 7 we find values for r^* that decrease from $20\,\mu$m for small values of $n\kappa^{-3}\xi^{-4}$ to $10\,\mu$m for the largest considered values.

It is instructive to compare r^* to the droplet radius, r_{Pe}, where the Pèclet number, Pe, of the droplet motion crosses one. Calculating $Pe = uL/D_d$ based on the sedimentation velocity $u = 2\Delta\rho\, g\, r_{Pe}^2/(9\eta)$, the droplet diameter $L = 2r_{Pe}$, and the Brownian droplet diffusivity $D_d = k_B\, T/(6\pi\eta\, r_{Pe})$ yields

$$Pe = \frac{8\pi}{3}\,\frac{\Delta\rho\, g}{k_B\, T}\, r_{Pe}^4\,. \tag{4.2}$$

It takes values $Pe \simeq 1$ for droplet radii $r_{Pe} = [k_B\,T/(8\pi\,\Delta\rho\,g)]^{1/4} \simeq 1.2\,\mu$m. In line with expectation, the bottleneck radius r^* is of the same order of magnitude, even though somewhat larger than r_{Pe}.

4.4. *The role of Ostwald ripening*

Wilkinson (2014) obtained (3.14) based on an analysis of the crossover from classical Ostwald ripening to the collection scenario also adopted in the present theory. His derivation does not provide a physical interpretation of the values of α, and was criticised in Rohloff *et al.* (2014) for not predicting physically sound values of Δt and the bottleneck radius, r^*.

Classical Ostwald ripening is encountered for $k = 1$. For this value (4.1) does not apply because (3.1) is obtained from the general equation (3.2) as a large k limit. Equation (3.2) approaches the asymptotic scaling solution of Ostwald ripening for $k = 1$ where $0 \leqslant a/\langle a\rangle \leqslant 3/2$ (Lifshitz & Slyozov 1961). Consequently, the largest droplets follow (3.2) with $k \simeq 3/2$, and (3.14) is recovered with a value α provided by (4.1) evaluated for $k = 3/2$. Hence, we find a value of $\alpha = 4.36$, which results in a prediction of Δt that is too large by a factor of about six.

The error in the prediction of the bottleneck radius is even more severe. When evaluating the expression

$$r^* = \left(\frac{12(k-1)^2 D^2 \sigma^2}{\varepsilon\kappa\xi}\right)^{1/7} \tag{4.3}$$

provided in Wilkinson (2014) and Rohloff *et al.* (2014), one obtains values in the order of $0.1\,\mu$m that are too small by two orders of magnitude. In particular, they are much smaller than the value where $Pe = 1$. These discrepancies rule out Ostwald ripening as a relevant contribution to growth in our experiments. In this respect our findings are fully analogous with the description of warm terrestrial rain where the effects of Ostwald ripening is also believed to be insignificant (Clement 2008).

4.5. *Predicting Δt for warm terrestrial rain*

It is instructive to evaluate, (3.13), for common situations in warm rain (Beard & Ochs 1993; Moran & Morgan 1997).

The number density of droplets has been determined in recent measurement campaigns (Ditas *et al.* 2012), yielding $n \simeq 4.7\times10^8\mathrm{m}^{-3}$. The material constants entering the settling velocity of the droplets are the density contrast of water and air, $\Delta\rho \approx 10^3\mathrm{kg/m}^3$, and the dynamic viscosity of air, $\mu = 1.8\times10^{-5}\mathrm{kg\,m^{-1}s^{-1}}$ at 10°C (Rogers & Yau 1989, p. 103). Given that the dynamic viscosity of air is much smaller than that of water, this provides a value $\kappa = 1.2\times10^8\mathrm{m^{-1}s^{-1}}$ [cf. (3.4)]. Moreover, the ramp rates ξ were estimated in Vollmer *et al.* (2014) to lie in the range $\xi = 5\times10^{-6}\ldots5\times10^{-5}\mathrm{s}^{-1}$. For a collection efficiency of $\varepsilon = 0.3$, equation (3.13) then provides time scales Δt in the range of 10 s and 30 s, and bottleneck radii of the order of $30\,\mu$m.

The value observed for the bottleneck radius matches expectation (Kostinski & Shaw 2005; Clement 2008). On the other hand, the value of Δt is too small as compared to experiments. This is extremely remarkable, because common estimates (Houghton 1959; Falkovich *et al.* 2002; Clement 2008) based on diffusive ripening processes and growth by collection tend to provide estimates that are rather too large. Indeed, this is also what one finds (Wilkinson 2014) when using (3.14) with $\alpha \simeq 1$. We attribute this discrepancy to limitations of the expression, (3.5), for the growth by collection. A model that only considers the size of the largest droplets tends to overestimate the growth speed of the droplets in this regime. After all, the collision frequency entering (3.5) should be based on the relative droplet velocity rather than on the falling velocity, (3.4), of the large

droplets. For the binary mixtures considered in the present paper the settling velocity of the small droplets is negligible such that the approximation holds. However, for systems with a large mass density contrast, $\Delta\rho$, i.e. in particular rain droplets in clouds, this is probably not justified. Follow-up work is in progress, where we incorporate information on the evolution of the full droplet distribution, in order to enhance the model to also cover this case.

5. Conclusion

In the present paper we have established a faithful description of the period, Δt, of episodic precipitation in binary mixtures. It is based on a low-dimensional model accounting only for the interplay of diffusive droplet growth and a runaway instability of the droplet size that arises when the largest droplets start to be effected by buoyancy. The model neither accounts for spatial degrees of freedom, nor for the droplet size distribution. In contrast to systems featuring reactive flow, the disregarding of spatial degrees of freedom is justified: for the nonlinear reactions terms that characterise phase separation, the convective mixing efficiently eliminates spatial inhomogeneities of the droplet size distribution (Benczik & Vollmer 2010, 2012). In addition, detailed knowledge about the droplet size distribution is not needed to predict Δt as long as there is some polydispersity in the distribution such that the largest droplets can effectively grow by collecting small droplets. The treatment of growth by collection has been inspired by models for initiation of warm rain (Houghton 1959; Beard & Ochs 1993; Kostinski & Shaw 2005). However, in contrast to earlier work we modelled the diffusive growth according to recently established models for aggregate growth in the presence of a sustained ramping of the droplet volume fraction (Clark *et al.* 2011; Vollmer *et al.* 2014). Combining the impact of the resulting diffusive growth, that is most effective for very small droplets, and growth by collection, that arises when the largest droplets reach a size where their Pèclet number surpasses one, provides a low-dimensional model for the dependence of Δt on the number density of droplets, n, the ramp rate, ξ, the collection efficiency, and material constants fixing the Stokes settling velocity of the droplets. This results in a master plot, figure 7, where data for various ramp rates and temperatures collapse on the theoretical prediction (3.13). The only free parameter in this fit is the collection efficiency that is expected to take values in the range between 0.1 and 1 (Beard & Ochs 1993). The theory also provides a relation, (3.2), between the droplet number density, n, the ramp rate, ξ, and material constants characterising diffusive droplet growth. This relation can be used to eliminate n from (3.13), thus obtaining a prediction (3.14) connecting $\xi^{3/7}\,\Delta t$ to a nontrivial combination of material constants that is a known function of temperature. The master plots shown in figure 8 demonstrate that this prediction is in quantitative agreement with a vast set of data obtained for repeated waves of precipitation in both phases of water/isobutoxyethanol and methanol/hexane mixtures. The data collapse establishes that the bottleneck of droplet growth quantitatively determines the time scale, Δt, of rain initiation in binary mixtures, and its parameter dependence. The bottleneck corresponds to the minimum of the droplet growth speed, arising for intermediate droplet radii where growth by diffusive collection of supersaturation is no longer effective, and collection of smaller droplets by large sedimenting droplets is not yet effective because buoyancy is still negligible. The time scale Δt amounts to a small multiple of the time needed to cross this bottleneck.

Follow-up work will address the evolution of the full droplet size distribution in order to explore how to reconcile the tendency of the distribution to become more monodisperse (Klein & Moisar 1963; Sugimoto 1992; Wallace & Hobbs 2006; Clark *et al.* 2011; Vollmer

et al. 2014) with the observation that growth of large droplets by collecting smaller ones works best for a large size mismatch (Wallace & Hobbs 2006). The excellent data collapse documented in figure 7 and figure 8 suggests that the approximation to still consider the small droplets in the runaway regime as Brownian particles seems to be well-justified for binary mixtures. In contrast, our estimate for warm terrestrial rain, section 4.5, suggests that our model predicts too small values for Δt due to an approximation of the droplet collection rates that need not hold for terrestrial rain. Extending the present work towards mixtures with a larger mass density contrast will allow us to systematically develop models addressing the emergence of precipitation in systems with a higher mass-density contrast between the coexisting phases. In particular, these generalisations of the model will allow us to address the growth of droplets in terrestrial (Kostinski & Shaw 2005; Grabowski & Wang 2013) and exo-planetary clouds (Marley *et al.* 2013).

Our views on the theoretical interpretation of the present data developed in intensive discussions with Michael Wilkinson, who also proposed to denote the investigated repeated nucleation and sedimentation cycles as episodic precipitation. In addition, we acknowledge very useful discussion with Charles Clement, Izabella Benczik, Itzhak Fouxon, Raymond Pierrehumbert, Raymond Shaw, Axel Seifert, and Valerio Lucarini, and we are grateful to Greg Bewley, Stephan Herminghaus, Jakob de Maeyer, and Marco Mazza for comments on the manuscript.

Appendix A. Material Constants

Figure 4 shows the period, Δt, of episodic precipitation for different ramp rates, ξ. Different data points for a given ramp rate are due to the drift of Δt when the pertinent material constants, D, σ, and $\kappa(\Delta\rho, \mu_b, \mu_d)$ change upon moving further away from the critical point. In the following we provide the temperature dependence of these material constants. We cite the data here as they were provided in the original literature (even when we are in doubt that they are accurate to six significant digits for our samples). Upon doing so we denote the mass fraction as ϕ^m and the molar fraction as ϕ^n, respectively. The resulting temperature dependence of the diffusion coefficient D, the Kelvin length σ provided by (3.3), and the sedimentation prefactor κ provided by (3.4), are summarised in figure 10 in order to give easy access to the constants appearing in the predictions (3.13) and (3.14). The temperature dependence translates to a time dependence when inverting the protocol $T(t)$ of the temperature ramp.

A.1. *Isobutoxyethanol and water*

The theoretical curves in figures 7 and 8 use data on material parameters from a variety of sources (Steinhoff & Woermann 1995; Aratono *et al.* 1990; Doi *et al.* 2000; Menzel *et al.* 2003; Douheret *et al.* 2002). The index $i \in \{\mathrm{IBE}, \mathrm{W}\}$ will be used to refer to material properties of IBE and water, respectively, and in accordance with the phase diagram, figure 3.a), the concentration are always given in terms of $\phi = \phi_{\mathrm{IBE}}$.

A.1.1. *Density (based on Doi* et al. *2000)*

The densities of the phases are determined by the composition, thermal expansion and molar excess volume,

$$\rho(\phi^m, T) = \left[\frac{\phi^m}{\rho_{\mathrm{IBE}}} + \frac{1-\phi^m}{\rho_{\mathrm{W}}} + \left(\frac{\phi^m}{M_{\mathrm{IBE}}} + \frac{1-\phi^m}{M_{\mathrm{W}}} \right) V_{\mathrm{E}}^n \right]^{-1}, \tag{A 1}$$

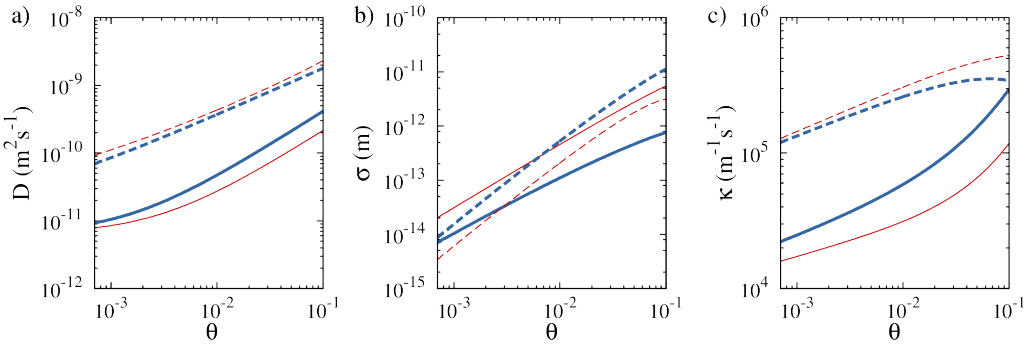

FIGURE 10. **Material constants**. a) The diffusion coefficient D, b) the Kelvin length σ, and c) the sedimentation prefactor κ as a function of the reduced temperature θ for IBE+W (solid lines) and M+H (dashed lines). The thick blue and the thin red lines show the dependence in the lower and the upper layer of the fluid mixtures, respectively.

	$\rho_i(T_0)$ [g cm^{-3}]	α_i [g cm^{-3} K^{-1}]
water	0.997043	0.2571×10^{-3}
IBE	0.886255	0.968×10^{-3}

TABLE 2. Densities and thermal expansion coefficients for water and IBE according to Doi *et al.* (2000).

where $\rho_i = \rho_i(T)$ are the (temperature-dependent) densities of the pure substances, M_i their molar masses, and $V_\mathrm{E}^n = V_\mathrm{E}^n(\phi^n)$ is the molar excess volume.

The molar masses, M_i are 18.01528 g/mol for water (PubChem 2013*a*) and 118.17416 g/mol for IBE (PubChem 2013*b*), respectively.

The temperature dependence of the density, $\rho_i(T)$, of the pure substances is linearly approximated around $T_0 = 25°\mathrm{C}$,

$$\rho_i(T) = \rho_i(T_0) - \alpha_i \, (T - T_0) \tag{A 2}$$

with fit parameters for ρ_i and α_i given in Table 2.

Moreover, the molar excess volume is fitted according to Doi *et al.* (2000):

$$V_\mathrm{E}^n(\phi^n) = \frac{\phi^n \, (1-\phi^n)}{1 - G \, \tilde{\phi}} \, \left(A_1 + A_2 \, \tilde{\phi} + A_3 \, \tilde{\phi}^2 \right) \tag{A 3}$$

$$\text{with} \quad \tilde{\phi} = 1 - 2\phi^n$$

$$\text{and} \quad G = 0.975\,,$$

$$A_1 = -3.079 \text{ cm}^3/\text{mol}\,,$$

$$A_2 = 1.801 \text{ cm}^3/\text{mol}\,,$$

$$A_3 = 0.839 \text{ cm}^3/\text{mol}\,.$$

A slight temperature dependence of these fit parameters was reported in Doi *et al.* (2000). However, it is so small that we need not take it into account here.

To get the dependence of the density difference on the reduced temperature the dependence $\phi(\theta)$ (coexistence curve) into (A 1).

	A [kg m^{-1} s^{-1}]	B	C [(° C)$^{-1}$]	D [° C]
water	1.002×10^{-3}	1.3272	0.001053	105
IBE	3.4×10^{-3}	1.7	0.001	110

TABLE 3. Data of Weast *et al.* (1988) for the fit coefficients for the viscosity of water and IBE, defined by (A 4). In both cases $T_0 = 20°\mathrm{C}$ is used as reference temperature.

A.1.2. *Viscosity (own measurements augmented by data of Weast* et al. *1988; Menzel* et al. *2003)*

We first provide the data of the pure phases, and then obtain the viscosity of the mixture by appropriate interpolation.

Following Weast *et al.* (1988) we describe the temperature dependence of the pure substances by

$$\mu_i(T) = A_i \, 10^{\frac{B_i\,(T_0-T)-C_i\,(T_0-T)^2}{T+D_i}} \,. \tag{A 4}$$

In Table 3 we provide the values for pure water provided in Weast *et al.* (1988), and parameters of a fit for IBE whose viscosity we determined with an Ubbelohde viscometer type 537 10/I made by Schott.

To interpolate the viscosities for a mixed phase of given mass fraction ϕ^m we use the composition-dependent viscosities at the reference temperature $T_r = 25°\mathrm{C}$ for a homogeneous mixture in the single-phase regime (Menzel *et al.* 2003). The data is fitted with a fifth order polynomial

$$\begin{aligned} \mu(\phi^m, T_r) &= -40.66\,(\phi^m)^5 + 103.44\,(\phi^m)^4 - 100.32\,(\phi^m)^3 \\ &\quad +39.35\,(\phi^m)^2 + 0.17\,\phi^m + 0.91 && \text{(A 5}a\text{)} \\ &= w_\mu(\phi^m)\;\mu_{\mathrm{IBE}}(T = 25°\mathrm{C}) + [1 - w_\mu(\phi^m)]\;\mu_{\mathrm{W}}(T = 25°\mathrm{C})\,, && \text{(A 5}b\text{)} \end{aligned}$$

where the latter equation *defines* the dimensionless, non-linear weight function w_μ that expresses $\mu(\phi^m, T = 25°\mathrm{C})$ as a function of the viscosities of the pure substances $\mu_{\mathrm{IBE}}(T = 25°\mathrm{C})$ and $\mu_{\mathrm{W}}(T = 25°\mathrm{C})$, respectively.

Assuming that this weight function is not varying substantially in the temperature range of our measurements, we can use the interpolation (A 5b) to determine the viscosity of the mixture also at other temperatures. After all, the temperature dependence $\mu_{\mathrm{IBE}}(T)$ and $\mu_{\mathrm{W}}(T)$ were provided by (A 4) with coefficients in Table 3. To check the strong assumption entering this interpolation,

$$\mu(\phi^m, T) = w_\mu(\phi^m)\;\mu_{\mathrm{IBE}}(T) + [1 - w_\mu(\phi^m)]\;\mu_{\mathrm{W}}(T)\,, \tag{A 6}$$

we measured the viscosity of the two coexisting phases at $T = 40°\mathrm{C}$. For both phases the prediction of (A 6) was accurate to within 2%. This is sufficient for our purposes.

A.1.3. *Diffusion coefficient (based on Steinhoff & Woermann 1995)*

The renormalisation group theory predicts that the diffusion coefficient vanishes when the critical point is approached. On the other hand, the renormalisation group theory is precise only in the vicinity of the critical point, and its application to interdiffusion coefficients has been a source of controversy (Sengers 1985; Das *et al.* 2006). For this reason we choose to rely upon interpolations of experimental data. We do not expect that our data follow the critical exponents because the temperatures in our experiments lie outside the critical region. Hence, we fitted the data of Steinhoff & Woermann (1995)

	a_0 [g cm^{-3}]	a_1 [g cm^{-3} K^{-1}]	a_2 [g cm^{-3} K^{-2}]
methanol	1.382	-3.135×10^{-3}	3.813×10^{-6}
hexane	0.6839	6.989×10^{-4}	-2.656×10^{-6}

TABLE 4. Coefficients of the density (Abbas *et al.* 1997).

with the following expression:

$$D_i(\theta) = D_\mathrm{c} + \delta_i\, \theta \tag{A 7}$$

with $D_\mathrm{c} = 6.4 \times 10^{-12}\mathrm{m}^2/\mathrm{s}$, $\delta_\mathrm{IBE} = 2.1 \times 10^{-9}\mathrm{m}^2/\mathrm{s}$ and $\delta_\mathrm{W} = 4.1 \times 10^{-9}\mathrm{m}^2/\mathrm{s}$.

A.1.4. *Interfacial tension (based on Aratono* et al. *1990)*

The interfacial tension vanishes at the critical temperature, and its dependence at higher temperatures can be represented by a power law

$$\gamma(\theta) = \gamma_0\, \theta^{\alpha_\gamma}\,, \tag{A 8}$$

where a fit to the data of Aratono *et al.* (1990) yields $\gamma_0 = 7.3 \times 10^{-4}\mathrm{N/m}$ and $\alpha_\gamma = 1.2$.

A.1.5. *Molar volume (based on Douheret* et al. *2002)*

According to Douheret *et al.* (2002) the molar volume V^n can be approximated by

$$V^n = \phi^n\, V^n_\mathrm{IBE} + (1 - \phi^n)\, V^n_\mathrm{W} \tag{A 9}$$

with $V^n_\mathrm{IBE} = 124\mathrm{cm}^3/\mathrm{mol}$ and $V^n_\mathrm{W} = 15.98\mathrm{cm}^3/\mathrm{mol}$.

A.2. *Methanol/hexane mixtures*

In this subsection the index $i \in \{M, H\}$ denotes material constants of the methanol and hexane, respectively, and concentrations refer to methanol, $\phi = \phi_\mathrm{M}$.

A.2.1. *Density (based on Abbas* et al. *1997; Orge* et al. *1997)*

The densities are again calculated according to (A 1). In this case the molar mass is 32.04186 g/mol for methanol (PubChem 2013*c*) and 86.17536 g/mol for hexane (PubChem 2013*d*). The temperature dependence of the pure substances amounts to (Abbas *et al.* 1997)

$$\rho_i(T) = a_0 + a_1\, T + a_2\, T^2 \tag{A 10}$$

with coefficients given in Table 4. The excess volume is expressed as (Orge *et al.* 1997)

$$V^n_E(\phi^n) = \phi^n\, (1 - \phi^n)\, \left[B_0 + B_1\tilde{\phi} + B_2\tilde{\phi}^2\right] \tag{A 11a}$$

$$\text{with} \quad \tilde{\phi} = 1 - 2\phi^n$$

$$\text{and} \quad B_0 = 2.0741\ \mathrm{cm}^3/\mathrm{mol},$$
$$B_1 = 0.3195\ \mathrm{cm}^3/\mathrm{mol},$$
$$B_2 = 1.7733\ \mathrm{cm}^3/\mathrm{mol}.$$

A.2.2. *Viscosity (based on Assael & Polimatidou 1994; Eicher & Zwolinski 1972; Orge* et al. *1997)*

We first provide the data of the pure phases, and then obtain the viscosity of the mixture by appropriate interpolation.

The viscosity of pure methanol (Assael & Polimatidou 1994) is

$$\mu_{\mathrm{M}}(T) = A\ \exp(B/T) \tag{A 12}$$

with $A = 8.203 \times 10^{-6}$Pa s and $B = 1251.4\,\mathrm{K}$.

For hexane our analysis is based on the kinematic viscosity ν_{H} provided in Eicher & Zwolinski (1972)

$$\nu_{\mathrm{H}}(T) = \nu' \left(\frac{T}{T'}\right)^{n} \exp\left(\frac{B(T'-T)}{(T'-T_0)(T-T_0)}\right) \tag{A 13}$$

with $n = -2.24057$, $B = 4.78496\,\mathrm{K}$ and $T_0 = 222.468\,\mathrm{K}$, reference viscosity $\nu' = 0.4604 \times 10^{-10}\mathrm{m}^2/\mathrm{s}$, and reference temperature $T' = 296.267\,\mathrm{K}$. Together with the density of hexane, which is provided in (A 10), this provides the dynamic viscosity $\mu_{\mathrm{H}} = \rho_{\mathrm{H}}\,\nu_{\mathrm{H}}$.

The viscosity of the mixture is obtained by interpolating based on the excess viscosity provided in Orge *et al.* (1997)

$$\mu(\phi^n, T) = \phi^n\,\mu_{\mathrm{M}}(T) + (1-\phi^n)\,\mu_{\mathrm{H}}(T) + \phi^n\,(1-\phi^n)\,[B_0 + B_1(1-2\,\phi^n)] \tag{A 14}$$

$$\text{with} \quad B_0 = -1.83 \times 10^{-4}\mathrm{kg\,m^{-1}\,s^{-1}}$$

$$B_1 = 0.91 \times 10^{-4}\mathrm{kg\,m^{-1}\,s^{-1}}\,.$$

A.2.3. *Diffusion coefficient (based on Clark & Rowley 1986)*

The dependence of the diffusion coefficient $D(\phi^n, \theta)$ on the concentration ϕ^n of the mixture and on the reduced temperature θ can be approximated by (Clark & Rowley 1986)

$$D(\phi^n, \theta) = A_0 + A_1\,\phi^n + A_2\,(\phi^n)^2 + A_3\,(\phi^n)^3 + A_4\,(\phi^n)^4 + A_\theta\,\theta^{0.68516} \tag{A 15}$$

$$\begin{aligned} \text{with} \qquad & A_0 = 3.2457 \times 10^{-9}\,\mathrm{m^2/s}, \\ & A_1 = -1.68497 \times 10^{-8}\,\mathrm{m^2/s}, \\ & A_2 = 3.63103 \times 10^{-8}\,\mathrm{m^2/s}, \\ & A_3 = -4.1949 \times 10^{-8}\,\mathrm{m^2/s}, \\ & A_4 = 2.223 \times 10^{-8}\,\mathrm{m^2/s}, \\ \text{and} \qquad & A_\theta = 2.5067 \times 10^{-9}\,\mathrm{m^2/s}\,. \end{aligned} \tag{A 16}$$

Similarly to the expression (A 7) the fit for the M+H mixture involves a constant background contribution, and the singular contribution expected from the theory of critical phenomena. Clark & Rowley (1986) fitted the composition dependence of the background contribution by a forth-order polynomial in ϕ^n, and introduced the term $A_5\,\theta^{0.68516}$ to account for the singular contribution to the diffusion. The latter term vanishes at $T = T_c$ with the appropriate critical scaling exponent, 0.68516.

A.2.4. *Interfacial tension (according to Abbas* et al. *1997)*

Data of interfacial tension (Abbas *et al.* 1997) are parametrised according to (A 8) with $\gamma_0 = 3.631 \times 10^{-2}\mathrm{N/m}$ and $\alpha_\gamma = 1.65$. This data lies beyond the critical region of $\theta < 10^{-2.5}$ where scaling with a critical exponents is expected (Abbas *et al.* 1997).

A.2.5. *Molar volume (according to Maruyama* et al. *1995)*

The molar volume is interpolated with (A 9) with $V^n = 41.1\text{cm}^3/\text{mol}$ for methanol and $V^n = 133.2\text{cm}^3/\text{mol}$ for hexane (Maruyama *et al.* 1995).

REFERENCES

Aarts, D.G., Dullens, R.P.A. & Lekkerkerker, H.N.W. 2005 Interfacial dynamics in demixing systems with ultralow interfacial tension. *New J. Phys.* **7**, 40.

Abbas, Shabira, Satherley, John & Penfold, Robert 1997 The liquid-liquid coexistence curve and the interfacial tension of the methanol-n-hexane system. *J. Chem. Soc. Farad Trans.* **93**, 2083–2089.

Aizpiri, Arturo G., Correa, José A., Rubio, Ramón G. & Peña, Mateo Dŕiaz 1990 Coexistence curve of methanol+n-heptane: Range of simple scaling and critical amplitudes. *Phys. Rev. B* **41**, 9003.

Aratono, M., Nakayama, S., Ikeda, N. & Motomura, K. 1990 Thermodynamic consideration on the interface formation of water and ethylene glycol isobutyl ether mixture. *Coll. Polymer Sc.* **268**, 877–82.

Assael, M. J. & Polimatidou, S. K. 1994 Measurements of the viscosity of alcohols in the temperature range 290–340 K at pressures up to 30 MPa. *Int. J. Thermophys.* **15** (1), 95–107.

Auernhammer, Günter K., Vollmer, Doris & Vollmer, Jürgen 2005 Oscillatory instabilities in phase separation of binary mixtures: Fixing the thermodynamic driving. *J. Chem. Phys.* **123**, 134511.

Beard, Kenneth V. & Ochs, Harry T. 1993 Warm-rain initiation: An overview of microphysical mechanisms. *J. Appl. Meteor.* **32**, 608–625.

Benczik, I.J. & Vollmer, J. 2010 A reactive-flow model of phase separation in fluid binary mixtures with continuously ramped temperature. *EPL* **91**, 36003.

Benczik, I.J. & Vollmer, J. 2012 A diffusion-induced transition in the phase separation of binary fluidmixtures subjected to a temperature ramp. *EPL* **100** (1), 16001.

Beysens, D., Guenoun, P. & Perrot, F. 1988 Phase separation of critical binary fluids under microgravity: Comparison with matched-density conditions. *Phys. Rev. A* **38**, 4173–4185.

Binder, K & Stauffer, D 1976 Statistical theory of nucleation, condensation and coagulation. *Adv. Phys.* **25**, 343–396.

Blyth, Alan M., Lowenstein, Jason H., Huang, Yahui, Cui, Zhiqiang, Davies, Stewart & Carslaw, Kenneth S. 2013 The production of warm rain in shallow maritime cumulus clouds. *Quart. J. Roy. Met. Soc.* **139**, 20–31.

Bray, Alan J. 1994 Theory of phase-ordering kinetics. *Adv. Phys.* **43**, 357 – 459.

Cashman, Katharine V. & Sparks, R. Stephen J. 2013 How volcanoes work: A 25 year perspective. *Geol. Soc. Am. Bull.* **125** (5–6), 664–690.

Cates, Michael E., Vollmer, Jürgen, Wagner, Alexander & Vollmer, Doris 2003 Phase separation in binary fluid mixtures with continuously ramped temperature. *Phil. Trans. Roy. Soc. (Lond.) Ser. A* **361**, 793–807.

Cau, Franco & Lacelle, Serge 1993 Late-stage phase separation and sedimentation in a binary liquid mixture. *Phys. Rev. E* **47**, 1429–1432.

Clark, Michael D., Kumar, Sanat K., Owen, Jonathan S. & Chan, Emory M. 2011 Focusing nanocrystal size distributions via production control. *Nano Lett.* **11**, 1976–1980.

Clark, W. M. & Rowley, R. L. 1986 The mutual diffusion coefficient of methanol-n-hexane near the consolute point. *AIChE Journal* **32** (7), 1125–1131.

Clement, Charles F. 2008 *Environmental Chemistry of Aerosols*, chap. Mass Transfer to Aerosols, pp. 49–89. Oxford: Blackwell Publishing.

Das, Subir K., Fisher, Michael E., Sengers, Jan V., Horbach, Jürgen & Binder, Kurt 2006 Critical dynamics in a binary fluid: Simulations and finite-size scaling. *Phys. Rev. Lett.* **97**, 025702.

Ditas, Florian, Shaw, Raymond A., Siebert, Holger, Simmel, Martin, Wehner, Birgit & Wiedensohler, Alfred 2012 Aerosols-cloud microphysics-thermodynamics-

turbulence: evaluating supersaturation in a marine stratocumulus cloud. *Atm. Chem Phys.* **12** (5), 2459–2468.

Doi, Hideshige, Tamura, Katsutoshi & Murakami, Sachio 2000 Thermodynamic properties of aqueous solution of 2-isobutoxyethanol at T= (293.15, 298.15, and 303.15) K, below and above LCST. *J. Chem. Thermodyn.* **32** (6), 729–741.

Douheret, Gerard, Davis, Michael I., Reis, Joao Carlos R., Fjellanger, Inger Johanne, Vaage, Marit Bo & Hoiland, Harald 2002 Aggregative processes in aqueous solutions of isomeric 2-butoxyethanols at 298.15 K. *Phys. Chem. Chem. Phys.* **4** (24), 6034–6042.

Eicher, Lawrence D. & Zwolinski, Bruno J. 1972 Molecular structure and shear viscosity. isomeric hexanes. *J. Phys. Chem.* **76** (22), 3295–3300.

Emmanuel, Simon & Berkowitz, Brian 2006 An experimental analogue for convection and phase separation in hydrothermal systems. *J. Geophys. Res.* **111**, B09103.

Falkovich, G., Fouxon, A. & Stepanov, M.G. 2002 Acceleration of rain initiation by cloud turbulence. *Nature* **419**, 151–154.

Farjoun, Yossi & Neu, John C. 2011 Aggregation according to classical kinetics: From nucleation to coarsening. *Phys. Rev. E* **83**, 051607.

Grabowski, Wojciech W. & Wang, Lian-Ping 2013 Growth of cloud droplets in a turbulent environment. *Ann. Rev. Fluid Mech.* **45**, 293–324.

Guyon, Etienne, Hulin, Jean-Pierre, Petit, Luc & Mitescu, Catalin D. 2001 *Physical Hydrodynamics*. Oxford: Oxford Univ. Press, translation from French: 'Hydrodynamique Physique', 1991.

Han, Weon S., Lu, M., McPherson, B. J., Keating, E. H., Moore, J., Park, E., Watson, Z. T. & Jung, N.-H. 2013 Characteristics of CO_2-driven cold-water geyser, crystal geyser in Utah: experimental observation and mechanism analyses. *Geofluids* **13** (3), 283–297.

Houghton, H. G. 1959 Cloud physics. *Science* **129**, 307–313.

Huang, John S., Goldburg, Walter I. & Bjerkaas, Allan W. 1974 Study of phase separation in a critical binary liquid mixture: spinodal decomposition. *Phys. Rev. Lett.* **32**, 921–923.

Ingebritsen, S. E. & Rojstaczer, S. A. 1993 Controls on geyser periodicity. *Science* **262** (5135), 889–92.

Iwanowski, I., Sattarow, A., Behrends, R., Mirzaev, S. Z. & Kaatze, U. 2006 Dynamic scaling of the critical binary mixture methanol-hexane. *J. Chem. Phys.* **124**, 144505.

Kalwarczyk, Tomasz, Ziebacz, Natalia, Fialkowski, Marcin & Holyst, Robert 2008 Late stage of the phase-separation process: Coalescence-induced coalescence, gravitational sedimentation, and collective evaporation mechanisms. *Langmuir* **24**, 6433 – 6440.

Klein, E. & Moisar, E. 1963 Elektronenmikroskopische und nephelometrische Untersuchungen über das Kornwachstum von Silberhalogenidkristallen. *Berichte Bunsenges. phys. Chem.* **67** (4), 349–355.

Kostinski, Alexander B. & Shaw, Raymond A. 2005 Fluctuations and luck in droplet growth by coalescence. *Bull. Am. Met. Soc.* **86**, 235–244.

Koyaguchi, Takehiro, Hallworth, Mark A., Huppert, Herbert E. & Sparks, R. Stephen J. 1990 Sedimentation of particles from a convecting fluid. *Nature* **343**, 447 – 450.

Lapp, Tobias, Rohloff, Martin, Vollmer, Jürgen & Hof, Björn 2012 Particle tracking for polydisperse sedimenting droplets in phase separation. *Exp. Fluids* **52**, 1187–1200.

Leubner, Ingo H. 2000 Particle nucleation and growth models. *Curr. Opinion Coll. Interf. Sc.* **5**, 151–159.

Lifshitz, E. M. & Pitaevskii, L. P. 1981 *Landau and Lifshitz Course of Theoretical Physics, Vol.10 : Physical Kinetics*. Oxford: Butterworth-Heimemann.

Lifshitz, Ilya M. & Slyozov, Vitaly V. 1961 The kinetics of precipitation from supersaturated solid solutions. *J. Phys. Chem. Solids* **19** (1–2), 35 – 50.

Marley, M., Ackerman, A., Cuzzi, J. & Kitzmann, D. 2013 Clouds and hazes in exoplanet atmospheres. In *Comparative Climatology of Terrestrial Planets* (ed. S.J. Mackwell, A.A. Simon-Miller, J.W. Harder & M.A. Bullock), pp. 367–391. University of Arizona Press.

Martin, Daniel & Nokes, Roger 1988 Crystal settling in a vigorously converting magma chamber. *Nature* **332**, 534 – 536.

Maruyama, K., Kawase, S., Tamaki, S. & Okazaki, H. 1995 Thermodynamic aspects of the Rayleigh and Brillouin scattering from a binary liquid mixture: The hexane-methanol system. *J. Phys. Chem.* **99** (26), 10644–10647.

McGraw, Robert & Liu, Yangang 2003 Kinetic potential and barrier crossing: A model for warm cloud drizzle formation. *Phys. Rev. Lett.* **90**, 018501.

Menzel, K., Mirzaev, S. Z. & Kaatze, U. 2003 Crossover behavior in micellar solutions with lower critical demixing point: Broadband ultrasonic spectrometry of the isobutoxyethanol-water system. *Phys. Rev. E* **68** (1), 011501.

Mirzaev, Sirojiddin Z., Heimburg, Thomas & Kaatze, Udo 2010 Critical behavior of polystyrene-cyclohexane: Heat capacity and mass density. *Phys. Rev. E* **82**, 061502.

Moran, Joseph H. & Morgan, Michael D. 1997 *Meteorolgy: The Atmosphere and the Science of Weather*, 5th edn. Upper Saddle River, NJ: Prentice-Hall.

Nakata, Mitsuo, Dobashi, Toshiaki, Kuwahara, Nobuhiro & Kaneko, Motozo 1982 Coexistence curve and diameter of the system ethylene glycol mono-isobutyl ether + water. *J. Chem. Soc. Farad Trans.* **78**, 1801–1810.

Nozawa, Koh, Delville, Marie-Hélène, Ushiki, Hideharu, Panizza, Pascal & Delville, Jean-Pierre 2005 Growth of monodisperse mesoscopic metal-oxide colloids under constant monomer supply. *Phys. Rev. E* **72**, 011404.

Orge, B., Iglesias, M., Rodrguez, A., Canosa, J. M. & Tojo, J. 1997 Mixing properties of (methanol, ethanol, or 1-propanol) with (n-pentane, n-hexane, n-heptane and n-octane) at 298.15 K. *Fluid Phase Equilibria* **133** (1-2), 213–227.

PubChem, National Center for Biotechnology Information 2013*a* Pubchem compound database. CID=962 (17 July 2013).

PubChem, National Center for Biotechnology Information 2013*b* Pubchem compound database. CID=521158 (17 July 2013).

PubChem, National Center for Biotechnology Information 2013*c* Pubchem compound database. CID=887 (17 July 2013).

PubChem, National Center for Biotechnology Information 2013*d* Pubchem compound database. CID=8058 (17 July 2013).

Rimbert, N., Claudotte, L., Gardin, P. & Lehmann, J. 2014 Modeling the dynamics of precipitation and agglomeration of oxide inclusions in liquid steel. *Ind. Eng. Chem. Res.* **53** (20), 8630–8639.

Rogers, Roddy R. & Yau, M. K. 1989 *A Short Course in Cloud Physics*, 3rd edn., *International Series in natural philosophy*, vol. 113. Pergamon Press, Oxford.

Rohloff, Martin, Lapp, Tobias & Vollmer, Jürgen 2014 Comment on "A test-tube model for rainfall" by Wilkinson Michael. *EPL* **108**, 30005.

Sam, Ebie M., Hayase, Yumino, Auernhammer, Günter K. & Vollmer, Doris 2011 Pattern formation in phase separating binary mixtures. *Phys. Chem. Chem. Phys.* **13**, 13333 – 13340.

Scholten, Elke, van der Linden, Erik & This, Herve 2008 The life of an anise-flavored alcoholic beverage: Does its stability cloud or confirm theory? *Langmuir* **24**, 1701–1706.

Sengers, Jan V. 1985 Transport properties of fluids near critical points. *Int. J. Thermophys.* **6**, 203.

Slezov, Vitaly V. 2009 *Kinetics of First-Order Phase Transitions*. Weinheim: Wiley-VCH.

Soltzberg, Leonard J., Bowers, Peter G. & Hofstetter, Christine 1997 A computer model for soda bottle oscillations: "The Bottelator". *J. Chem. Edu.* **74** (6), 711 – 714.

Sparks, R. Stephen, Huppert, Herbert E., Kozaguchi, Takehiro & Hallwood, Mark A. 1993 Origin of modal and rhythmic igneous layering by sedimentation in a convecting magma chamber. *Nature* **361**, 246–249.

Steinhoff, B. & Woermann, D. 1995 Slowing down of the kinetics of liquid/liquid phase separation along the binodal curve of a binary liquid mixture with a miscibility gap approaching the critical point. *J. Chem. Phys.* **103** (20), 8985–8992.

Stevens, Björn & Feingold, Graham 2009 Untangling aerosol effects on clouds and precipitation in a buffered system. *Nature* **461**, 607–613.

Stevens, Björn & Seifert, Axel 2008 Understanding macrophysical outcomes of microphysical choices in simulations of shallow cumulus convection. *J. Met. Soc. Japan. Ser. II* **86A**, 143–162.

Sugimoto, Tadao 1992 The theory of the nucleation of monodisperse particles in open systems and its application to AgBr systems. *J. Coll. Interf. Sc.* **150** (1), 208 – 225.

Taylor, T.D. & Acrivos, Andreas 1964 On the deformation and drag of a falling viscous drop at low reynolds numbers. *J. Fluid Mech.* **18** (3), 466 – 476.

Tokano, Tetsuya 2011 Precipitation climatology on Titan. *Science* **331**, 1393 – 1394.

Tokuyama, M. & Enomoto, Y. 1993 Theory of phase-separation dynamics in quenched binary mixtures. *Phys. Rev. E* **47** (2), 1156.

Toramaru, Atsushi & Maeda, Kazuki 2013 Mass and style of eruptions in experimental geysers. *J. Volcanology Geothermal Res.* **257**, 227–239.

Vollmer, Doris, Strey, R. & Vollmer, Jürgen 1997 Oscillating phase separation in microemulsions I: Experimental observation. *J. Chem. Phys.* **107** (9), 3619–3626.

Vollmer, Jürgen, Auernhammer, Günter K. & Vollmer, Doris 2007 Minimal model for phase separation under slow cooling. *Phys. Rev. Lett.* **98**, 115701.

Vollmer, Jürgen, Papke, Ariane & Rohloff, Martin 2014 Ripening and focusing of aggregate size distributions with overall volume growth. *Front. Physics* **2**, 18.

Vollmer, Jürgen & Vollmer, Doris 1999 Cascade nucleation in the phase separation of amphiphilic mixtures. *Faraday Disc.* **112**, 51–62.

Wallace, John M. & Hobbs, Peter V. 2006 *Atmospheric Science – An Introductory Survey*, *International Geophysics Series*, vol. 92. Burlington, MA: Academic Press.

Weast, Robert C., Astle, Melvin J. & Beyer, William H., ed. 1988 *CRC Handbook of Chemistry and Physics*, 69th edn. CRC Press, Inc. Boca Raton, Florida.

Wilkinson, Michael 2014 A test-tube model for rainfall. *EPL* **106**, 40001.

Woods, Andrew W. 2010 Turbulent plumes in nature. *Ann. Rev. Fluid Mech.* **42**, 391–412.

Wylie, Jonathan J., Voight, Barry & Whitehead, J. A. 1999 Instability of magma flow from volatile-dependent viscosity. *Science* **285** (5435), 1883–1885.

Yuan, Quan, Thomas, Brian G. & Vanka, S. P. 2004 Study of transient flow and particle transport in continuous steel caster molds: Part ii. particle transport. *Metall. Mat. Trans. B* **35**, 703–714.

Zhang, Youxue & Kling, George 2006 Dynamics of lake eruptions and possible ocean eruptions. *Annu. Rev. Earth Planet. Sci.* **34**, 293–324.

Zhang, Youxue & Xu, Zhengjiu 2008 "Fizzics" of bubble growth in beer and champagne. *Elements* **4** (4), 47 – 49.

Zhang, Y. X. 1996 Dynamics of CO_2-driven lake eruptions. *Nature* **379** (6560), 57–59.